

Published in final edited form as:

*J Comput Neurosci.* 2014 August ; 37(1): 9–28. doi:10.1007/s10827-013-0483-3.

## Frequency preference in two-dimensional neural models: a linear analysis of the interaction between resonant and amplifying currents

Horacio G. Rotstein and Farzan Nadim

Department of Mathematical Sciences, New Jersey Institute of Technology

Department of Biological Sciences, New Jersey Institute of Technology, and Rutgers University-Newark

Horacio G. Rotstein: horacio@njit.edu; Farzan Nadim: farzan@njit.edu

### Abstract

Many neuron types exhibit preferred frequency responses in their voltage amplitude (resonance) or phase shift to subthreshold oscillatory currents, but the effect of biophysical parameters on these properties is not well understood. We propose a general framework to analyze the role of different ionic currents and their interactions in shaping the properties of impedance amplitude and phase in linearized biophysical models and demonstrate this approach in a two-dimensional linear model with two effective conductances  $g_L$  and  $g_1$ . We compute the key attributes of impedance and phase (resonance frequency and amplitude, zero-phase-frequency, selectivity, etc.) in the  $g_L$ - $g_1$  parameter space. Using these attribute diagrams we identify two basic mechanisms for the generation of resonance: an increase in the resonance amplitude as  $g_1$  increases while the overall impedance is decreased, and an increase in the maximal impedance, without any change in the input resistance, as the ionic current time constant increases. We use the attribute diagrams to analyze resonance and phase of the linearization of two biophysical models that include resonant ( $I_h$  or slow potassium) and amplifying currents (persistent sodium). In the absence of amplifying currents, the two models behave similarly as the conductances of the resonant currents is increased whereas, with the amplifying current present, the two models have qualitatively opposite responses. This work provides a general method for decoding the effect of biophysical parameters on linear membrane resonance and phase by tracking trajectories, parametrized by the relevant biophysical parameter, in pre-constructed attribute diagrams.

### Keywords

Resonance; subthreshold oscillations; zero phase frequency; impedance; model neuron

## Introduction

A variety of rhythmic oscillations are observed in different areas of the central nervous system which are known to be critical in cognitive and motor behaviors and are thought to emerge from the coordinated activity of the neurons in the respective networks (Gray 1994; Marder and Calabrese 1996; Wang 2010). Recent work suggests that the frequency of the network oscillations may crucially depend on the intrinsic preferred frequencies of the constituent neurons (Lau and Zochowski 2011; Wu et al. 2001; Tohidi and Nadim 2009; Ledoux and N. 2011; Moca et al. 2012; Sciamanna and Wilson 2011). These preferred frequencies arise in different contexts: the ability of a neuron to generate subthreshold oscillations at a particular frequency, often in response to a DC current input (Dickson and Alonso 1997; Lampl and Yarom 1997; Schmitz et al. 1998; Reboreda et al. 2003); the tendency of a neuron to produce subthreshold membrane potential resonance, a peak in the impedance amplitude in response to an oscillatory input current at a non-zero (resonant) frequency (Hutcheon and Yarom 2000); or membrane potential oscillations with zero phase lag in response to an oscillatory current input at a specific frequency (zero-phase-frequency).

The properties of membrane resonance has been investigated in various systems (Gutfreund et al. 1995; Llinás and Yarom 1986; Reboreda et al. 2003; Schreiber et al. 2004; Hu et al. 2002; Reinker et al. 2004; Tohidi and Nadim 2009; Dembrow et al. 2010; Narayanan and Johnston 2007) but the biophysical mechanisms underlying the generation of membrane resonance and its relationship to suprathreshold oscillations are not well understood (Richardson et al. 2003). Membrane resonance results from a combination of low- and high-pass filter mechanisms that also require a negative feedback effect (Hutcheon and Yarom 2000). The passive membrane currents typically act as a low-pass filter, and the so-called resonant voltage-gated currents oppose voltage changes at low frequencies and act as a high-pass filter, thus creating a preferred frequency band. Other voltage-gated ionic currents, labeled amplifying currents, do not produce resonance but generate a positive feedback effect that amplifies voltage changes and hence make existing resonance more pronounced (Hutcheon and Yarom 2000).

Although many studies have examined the impedance amplitude, much less attention has been paid to the phase of impedance which determines the phase of the subthreshold voltage response to oscillatory input currents (Richardson et al. 2003). In a linear approximation, as the amplitude of the oscillatory input increases, the phase of the output determines the phase at which the neuron first reaches threshold. This provides a first-order measure of the spiking phase of the neuron with respect to the input. For linear *RLC* circuits in series, this phase is zero at the resonant frequency. On the other hand, for *RLC* circuits in parallel, such as neural circuits, the zero-phase and the resonant frequencies do not necessarily coincide. We refer to the phase corresponding to the resonant frequency as the resonant phase, to the occurrence of a zero-phase voltage output at a positive input frequency as the zero-phase-frequency ( $f_{phase}$ ). Although  $f_{phase}$  is often measured experimentally (Gutfreund et al. 1995) and its importance for synchronization has been explored (Fuhrmann et al. 2002), the mechanisms underlying the occurrence of the zero-phase-frequency in biophysical neuronal systems have not been carefully investigated.

It is clear that the parameters of resonant and amplifying ionic currents shape the impedance and phase profiles but the relationship between these factors is far from intuitive. For instance, as we show in this study, increasing the maximal conductance of a so-called resonant current may lead to an increase or decrease of the maximal impedance value depending on the properties of this ionic current. As such, the characterization of the impedance and phase profiles (and the corresponding membrane resonance frequency and zero-phase-frequency) in terms of the properties of the ionic current parameters can provide valuable information on how interactions among biophysical properties of neurons may lead to emergent preferred frequencies.

The existence of subthreshold oscillations implies the presence of an intrinsic time scale in the neuron that is comparable in magnitude to the subthreshold oscillation period. The resonant frequency, on the other hand, reflects an emergent time scale which is a property of the interaction between the neuron and the input it receives. Intrinsic subthreshold oscillations and subthreshold resonance are related (Lampf and Yarom 1997) but are not equivalent phenomena. Linear models, for instance, may exhibit one but not the other (Richardson et al. 2003). Similarly, emergent time scales may be different from the neuron's intrinsic time scale, and are expected to be more relevant in the communication of subthreshold activity to the spiking and network activity. For instance, with large enough DC current, spikes are more likely to occur at the subthreshold oscillation peaks, whereas, with increased amplitude levels of an oscillatory input, spikes are more likely to occur at the resonant phase and inherit the resonant frequency.

In this paper we investigate the biophysical mechanisms underlying the emergence of the resonance and zero-phase-frequencies in two-dimensional models. In particular, we examine the role that different ionic currents and their associated time constants play in determining the resonant and zero-phase-frequencies and in shaping other relevant properties of a neuron's voltage response to oscillatory inputs. Our study consists of two parts. First we investigate the basic mechanisms of generation of resonance and zero-phase-frequency in a reduced two-dimensional linear model with two effective dimensionless conductances, a leak conductance  $g_L$  and a “resonant” conductance  $g_1$  (Richardson et al. 2003). This reduced system represents a linearization of a non-dimensionalized two-variable conductance-based model. We construct diagrams of the basic attributes (resonant and zero-phase-frequencies, amplitude, etc.) of the impedance and phase profiles in the  $g_L - g_1$  parameter space. We then investigate the effect of  $g_L$  and  $g_1$  on these attributes by exploring changes in their properties along horizontal (constant  $g_1$ ) and vertical (constant  $g_L$ ) lines in the corresponding attribute diagrams. In these reduced linear models, the kinetics of the resonant gating variable is not explicit but included in the effective conductances (Richardson et al. 2003). Additionally, we show that the effect of the corresponding time constants can be examined in the attribute diagrams along oblique lines in the  $g_L - g_1$  parameter space.

In the second part of the study we use the attribute diagrams mentioned above to investigate the mechanisms of generation of resonance and zero-phase-frequency in two-dimensional linearized conductance-based models. We consider two types of models, each with a resonant current. In the first model, the resonant current is a hyperpolarization-activated inward current  $I_h$  (Haas and White 2002; Hutcheon et al. 1996; Schreiber et al. 2004). In the

second model, the resonant current is a slow potassium current  $I_{Ks}$  activated by depolarization (Gutfreund et al. 1995). In each model we also examine the effect of a fast amplifying current  $I_P$  (Haas and White 2002; Hutcheon et al. 1996; Schreiber et al. 2004; Gutfreund et al. 1995) considered here with instantaneous kinetics. The study of the interaction between two distinct resonant currents with slow dynamics leads to models with at least three variables and is outside the scope of this paper. Changes in the biophysical conductances associated with these currents are reflected in changes in the effective conductances  $g_L$  and  $g_1$ . The model nonlinearities are captured by nonlinear trajectories in the  $g_L - g_1$  parameter space as one of the biophysical conductances change. We show that, although both  $I_h$  and  $I_{Ks}$  are resonant currents, the dependence of the resonance attributes on the biophysical conductances, in particular, the mechanisms underlying the amplification of the voltage responses are qualitatively different.

## Methods

### Conductance-based models

In this paper we consider biophysical (conductance-based) models of Hodgkin-Huxley type (Hodgkin and Huxley 1952). The current-balance equation is given by

$$C \frac{dV}{dt} = -I_L - \sum_k I_{x_k} + I_{app} + I_{in}(t) \quad (1)$$

where  $V$  is the membrane potential (mV),  $t$  is time (msec),  $C$  is the membrane capacitance ( $\mu\text{F}/\text{cm}^2$ ),  $I_{app}$  is the applied DC current ( $\mu\text{A}/\text{cm}^2$ ),  $I_L = G_L(V - E_L)$  is the leak current, and  $I_{x_k}$  are generic expressions for ionic currents of the form

$$I_x = G_x x (V - E_x) \quad (2)$$

with maximal conductance  $G_x$  ( $\text{mS}/\text{cm}^2$ ) and reversal potentials  $E_x$  (mV). All gating variables  $x$  follow a first order differential equation of the form

$$\frac{dx}{dt} = \frac{x_\infty(V) - x}{\tau_x(V)} \quad (3)$$

where  $x_\infty(V)$  and  $\tau_x(V)$  are, respectively, the voltage-dependent activation/inactivation curves and time constants. The function  $I_{in}(t)$  is a time-dependent input current (in  $\mu\text{A}/\text{cm}^2$ ). For sinusoidal input currents, we use the following notation

$$I_{in}(t) = A_{in} \sin(\omega t) \text{ with } \omega = \frac{2\pi f}{T} \quad (4)$$

Where  $T = 1000$  msec and  $f$  is in Hz.

The generic ionic currents (Eq. (2)) we consider here are restricted to have a single gating variable  $x$  and are linear in  $x$ . This choice is motivated by the persistent sodium current  $I_P$ , hyperpolarization-activated inward current  $I_h$  and slow M-type potassium current  $I_{Ks}$  found in a variety of neurons that exhibit subthreshold resonance (Schreiber et al. 2004; Acker et

al. 2003; Rotstein et al. 2006). Ionic currents of this form have been used in a variety of other models (Morris and Lecar 1981; Rinzel and Ermentrout 1998). The methods we use in this paper can be easily adapted for currents with two gating variables and gating variables raised to powers higher than 1.

We focus on two-dimensional models that describe the dynamics of voltage  $V$  and a gating variable  $x_1$ , respectively. Additional currents whose gating variables evolve on a fast time scale (faster than all other variables), such as persistent sodium currents, can be included by using the adiabatic approximation,  $x_k = x_{k,\infty}(V)$ . Here we consider one such additional (generic) current  $I_{x_2}$  with  $x_2 = x_{2,\infty}(V)$ . Additional fast currents can be considered without significantly changing the formalism used here.

### Linearized conductance-based models

Linearization of conductance-based models around a stable fixed-point  $(\bar{V}, \bar{x}_1)$  with  $\bar{V}$  below threshold for spike generation is a standard procedure (Ermentrout and Terman 2010). In its simplest form, it consists of substituting the right hand side of Eqs. (1) and (3) by their first order Taylor expansions calculated at the fixed point.

Here we follow Richardson et al. (Richardson et al. 2003) and linearize the autonomous part of system (1)–(3) around the fixed-point  $(\bar{V}, \bar{x}_1)$  for the isolated system ( $I_{in}(t) = 0$ ) by defining

$$\nu = V - \bar{V}, w_1 = \frac{x_1 - \bar{x}_1}{x'_{1,\infty}(\bar{V})} \quad (5)$$

where  $\bar{x}_1 = x_{1,\infty}(\bar{V})$ . The linearized equations are given by (Richardson et al. 2003)

$$C \frac{d\nu}{dt} = -g_L \nu - g_1 w_1 + I_{in}(t) \quad \bar{\tau}_1 \frac{dw_1}{dt} = \nu - w_1 \quad (6)$$

where the effective leak and ionic conductances and time constants are defined by

$$g_L = G_L + G_1 + G_2 + g_2 \quad G_1 = G_{x_1} x_{1,\infty}(\bar{V}) \quad G_2 = G_{x_2} x_{2,\infty}(\bar{V}) \quad g_2 = G_{x_2} x'_{2,\infty}(\bar{V})(\bar{V} - E_{x_2}) \quad (7)$$

$$g_1 = G_{x_1} x'_{1,\infty}(\bar{V})(\bar{V} - E_{x_1}), \bar{\tau}_1 = \tau_{x_1}(\bar{V}) \quad (8)$$

respectively. Note that the effective leak conductance  $g_L$  includes components from both the biophysical leak conductance  $G_L$  and the voltage-dependent ionic conductances: the slow ionic currents contributes a single term  $G_1$  whereas the fast current  $I_{x_2}$  contributes two terms,  $G_2$  and  $g_2$ .

The effective ionic conductance  $g_1$  can be either positive or negative. The sign of  $g_1$  determines whether the associated gating variable is resonant ( $g_1 > 0$ ) or amplifying ( $g_1 < 0$ ) (Richardson et al. 2003; Hutcheon and Yarom 2000). In our discussion, we will limit the values of  $g_1$  to the positive range which produces resonance. Note that  $g_2$ , the last term of

$g_L$  may also be positive or negative, depending on whether  $V > E_{x2}$ , and is of the same form as  $g_1$ . Thus, if  $g_2$  is negative, the fast current is amplifying.

Note that the gating variable  $w_1$  in (5) has units of voltage. Note also that the linearization process described above is not restricted to ionic currents of the form (2) and can be applied to models with an arbitrary number of ionic currents and any voltage-dependent time constant (Richardson et al. 2003).

System (6) can be rescaled in order to reduce the number of parameters (from four to two) that effectively govern its dynamics with no loss of information. We follow (Richardson et al. 2003) and define the following dimensionless time and parameters

$$\hat{t} = \frac{t}{\bar{\tau}_1}, \gamma_L = \frac{g_L \bar{\tau}_1}{C}, \gamma_1 = \frac{g_1 \bar{\tau}_1}{C}. \quad (9)$$

Substituting into (6) we obtain

$$\frac{d\nu}{d\hat{t}} = -\gamma_L \nu - \gamma_1 w_1 + \hat{I}_{in}(\hat{t}) \quad \frac{dw_1}{d\hat{t}} = \nu - w_1 \quad (10)$$

where

$$\hat{I}_{in}(\hat{t}) = \hat{A}_{in} \sin(2\pi f \hat{t} / \hat{T}) \text{ with } \hat{A}_{in} = \frac{A_{in} \bar{\tau}_1}{C} \quad (11)$$

with  $\hat{T} = T/\tau_1 = 1000/\tau_1$ . Note that  $[f] = \text{Hz}$ , and  $[\nu] = [w_1] = V$ . We refer to  $\gamma_L$  and  $\gamma_1$  as the dimensionless effective conductances. We will use dimensionless variables and parameters in Figs. 1–6.

## Impedance and impedance-like functions

The voltage response of a linear system receiving sinusoidal current inputs of the form (4) is given by

$$V_{out}(t; f) = A_{out}(f) \sin(\omega t - \phi(f)) \quad (12)$$

where  $\phi(f)$  is the phase offset (time difference between the peaks of the input current and the output voltage normalized by  $2\pi$ ) and  $\omega$  is given by the second equation in (4). Linear systems exhibit membrane (amplitude) resonance, if there is a peak in ratio of the output voltage and input current amplitudes:

$$Z(f) = \frac{A_{out}(f)}{A_{in}} \quad (13)$$

at some positive (resonant) frequency  $f_{res}$ , and zero-phase-frequency, if the phase offset  $\phi(f)$  vanishes at some positive frequency  $f_{phase}$ . We calculate the phase as the time difference between the output voltage and input current peaks normalized by the oscillation period. Henceforth, we will refer to the amplitude of impedance as impedance.

Figs. 1A and 1B show two representative graphs for the impedance profile of a low-pass filter RC model (panel A) and a band-pass filter model (panel B) exhibiting resonance at  $f = f_{res}$ . We will use four parameters to characterize impedance profiles:

- i. the resonant frequency  $f_{res}$ ,
- ii. the maximum impedance  $Z_{max} = Z(f_{res})$ ,
- iii. the resonance amplitude or power  $Q_Z = Z_{max} - Z(0)$ , and
- iv. the characteristic right-band-width  $\Lambda_{1/2}$  defined as the range of values of  $f \geq f_{res}$  such that  $Z(f) \geq Z_{max}/2$ .

$\Lambda_{1/2}$  provides information about the selectivity of the neuron to input frequencies. The smaller the value of  $\Lambda_{1/2}$ , the higher the selectivity, i.e., the impedance profile is peakier around the resonant frequency  $f_{res}$ . The choice of  $1/2$  is arbitrary and other values can be used. The restriction  $f \geq f_{res}$  is useful for comparison between cases where  $Z(0) > Z_{max}/2$  in one or more of the impedance profiles. In these cases, a “full” bandwidth will not be representative of the difference between impedance profiles. For a low-pass filter RC cell as in Fig. 1A,  $f_{res} = 0$  and  $Q_Z = 0$ .

Figs. 1C and 1D show two representative graphs for the phase ( $\phi$ ). They both approach  $\pi/2$  for large values of  $f$ . The phase in panel C is always increasing and positive; the voltage response is always delayed by at most one quarter of a cycle. The phase in panel D, on the other hand, is negative for  $f < f_{phase}$  and positive for larger values of  $f$ . The negative phase can be interpreted as the response leading the input. For  $f = f_{phase}$ , voltage response and input are in phase, so  $f_{phase}$  represents the zero-phase-frequency. We characterize the phase profile with an additional parameter  $\phi_{min}$  measuring the minimum phase.

In this paper we consider sinusoidal current inputs of the form (4) where  $A_{in}$  is a non-negative constant and the frequency  $f$  is measured in number of oscillations per 1000 units of time. For dimensional consistency with most experimental measurements, in Figs. 8–12, time  $t$  is expressed in milliseconds and  $f$  is measured in Hz.

## Results

### 1. Generation of resonance and zero-phase-frequency in two-dimensional linear models

In the first part of the Results we consider the 2D linear system (6) and sinusoidal current inputs  $I_{in}(t)$  of the form (4) with constant values of  $A_{in}$ . Because the system is linear, without loss of generality, we assume  $A_{in} = 1$ . For simplicity in the notation, we drop the “bar” from  $\tau_1$  and the “hat” from  $t$  and other parameters in (6) and (10). The eigenvalues, impedance, and resonant frequency for system (6) can be calculated from Eqs. (18), (21) and (22) in Appendix A by substituting  $a = -g_L C^{-1}$ ,  $b = -g_1 C^{-1}$ ,  $c = \tau_1^{-1}$ , and  $d = -\tau_1^{-1}$ . Alternatively, one can use the rescaled system (10) and compute the eigenvalues, impedance, and resonant frequency ( $r_{1,2}$ ,  $\hat{Z}$  and  $\hat{\omega}_{res}$  respectively) by substituting  $a = -\gamma_L$ ,  $b = -\gamma_1$ ,  $c = 1$  and  $d = -1$  in Eqs. (18), (21) and (22) of Appendix A. This information can then be used in the two-dimensional parameter space of effective conductances to investigate the effects of the biophysical parameters  $g_L$ ,  $g_1$ ,  $\tau_1$ , and  $C$  using



$$r_{1,2} = \frac{\hat{r}_{1,2}}{\tau_1}, Z(\omega) = \frac{\tau_1}{C} \hat{Z}(\tau_1 \omega), \text{ and } f_{res} = \frac{\hat{\omega}_{res}}{\tau_1} \frac{1000}{2\pi}. \quad (14)$$

For  $C = 1$  and  $\tau_1 = 1$ ,  $g_L = \gamma_L$  and  $g_1 = \gamma_1$  the two systems (6) and (10) are equivalent. Without loss of generality, we let  $C = 1$  and only consider the effects of changing  $\tau_1$ . Changes in  $\tau_1$  affect the magnitude of the eigenvalues but not their sign. These changes, therefore, do not affect the stability properties of the autonomous system but do affect, for instance, the natural frequency  $f_{nat}$  (when the autonomous system exhibits damped oscillations). Changes in  $\tau_1$  also affect the shape of the impedance function and the resonant frequency as will be discussed.

In Fig. 2A1 (magnified in 2A2) we show the stability diagram for the 2D linear system (6) with  $\tau_1 = 1$ . This diagram is similar to that presented in (Richardson et al. 2003). The blue curves separate regions in parameter space with different stability properties or distinct fixed point types (focus, node or saddle). The system is stable in the regions marked with blue symbols and unstable in regions marked with red. The green curve, referred to as the resonance curve, separates the regions in parameter space for which the system exhibit resonance (shaded green) and exhibit no resonance. Note that the regions in parameter space where the system exhibits intrinsic (damped) oscillations and resonance do not coincide (Richardson et al. 2003). In particular, resonance can occur in the absence of intrinsic oscillations where the fixed point is a node.

Representative impedance profiles show a variety of possible resonant behaviors (Figs. 2B to 2E). For  $\gamma_1 = 0$ , the first equation in the 2D linear system is independent of  $w_1$ ; the system has no resonance and simply describes a low-pass filter (Fig. 2B). As  $\gamma_L$  increases,  $Z_{max}(=Z(0))$  decreases (and  $\Lambda_{1/2}$  increases linearly; not shown). In this case, the phase  $\phi$  shows a delayed response for all values of  $\gamma_L$  but this delay decreases as  $\gamma_L$  increases (not shown). The expression of resonance in this system occurs when  $\gamma_1 > 0$ . For any fixed positive value of  $\gamma_1$ , increasing the value of  $\gamma_L$  results in an increase in the value of the resonance frequency  $f_{res}$  and a concomitant decrease in  $Z_{max}$  (Figs. 2C and 2D). Note, however, that resonance can occur with  $\gamma_L = 0$  (Fig. 2E).

**An increase in  $g_1$  generates resonance by an unbalanced decrease in  $Z_{max}$  and  $Z(0)$** —In order for the 2D linear system to exhibit resonance, the value of  $\gamma_1$  has to be in the resonant region above the resonance curve in Fig. 2A. For small enough values of  $\gamma_1$ , the system acts as a low-pass filter similar to the  $\gamma_1 = 0$  case described above. For resonance to emerge, a difference between  $Z_{max}$  and  $Z(0)$  (hence, a positive value of  $Q_Z = Z_{max} - Z(0)$ ) has to be generated as  $\gamma_1$  crosses the resonance curve. Figs. 3A and 3B show that, below the resonance curve, both the  $Z_{max}$  (and  $Z(0)$ ) level curves are almost linear and parallel to the line  $\gamma_1 + \gamma_L = 1$ , and they also nearly coincide (e.g., see Fig. 3C for  $\gamma_1 < 0.5$ ). Above the resonance curve, the  $Z_{max}$  level sets are no longer linear while the  $Z(0)$  level sets remain linear. Thus, as  $\gamma_1$  increases along vertical lines in  $\gamma_L - \gamma_1$  parameter space, resonance emerges because  $Z(0)$  decreases faster than  $Z_{max}$  (Figs. 3C and 3B inset). The difference ( $Q_Z$ ) is more attenuated for larger values of  $\gamma_L$  (Fig. 3B inset).



The resonance line is marked by a peak in the half-band-width  $\Lambda_{1/2}$  in the  $\gamma_L - \gamma_1$  parameter space as  $\gamma_1$  increases (Figs. 3E and 3F). As  $\gamma_1$  increases further,  $\Lambda_{1/2}$  settles into an almost constant value. The selectivity of resonance is therefore independent of  $\gamma_1$  for large enough values of  $\gamma_1$  (Fig. 3F). In contrast,  $\Lambda_{1/2}$  increases monotonically with  $\gamma_L$  (Fig. 3G).

**An increase in  $g_L$  generates low amplitude resonance**—Resonance occurs for all values of  $\gamma_L$  within the stability region for the underlying autonomous system, provided  $\gamma_1$  is large enough to be above the resonance curve (Fig. 2A, green region). For smaller values of  $\gamma_1$  (as in Fig. 2C), resonance can be generated by decreasing  $\gamma_L$  along horizontal lines that cross the resonance curve (solid gray curve in Figs. 3A–B). Along these lines, both  $Z_{max}$  and  $Z(0)$  decrease (as  $1/\gamma_L$ ) but at a slightly different pace (Fig. 3D), thus generating resonance. The resonance generated by this mechanism is much weaker as compared to the one described above for increasing values of  $\gamma_1$  in the sense that  $Q_Z$  is much smaller (Fig. 3B inset). This is because, as  $\gamma_L$  decreases, both  $Z_{max}$  and  $Z(0)$  change almost in parallel (e.g., Fig. 3D; also compare Figs. 3A and 3B).

**A decrease in  $g_L$  amplifies the voltage response and decreases  $f_{res}$** —A decrease in the effective leak conductance  $g_L$  (Eq. (7)) can be caused by a decrease in the biophysical leak conductance  $G_L$ , a decrease in the ionic conductances  $G_1$  and  $G_2$ , or an increase in the fast ionic conductance  $g_2$  when the associated gating variable is amplifying ( $g_2 < 0$ ; see Methods). In the latter case there is a competition between the relative magnitudes of the last two terms in Eq. (7). In some cases, as with the biophysical model we discuss later in this paper, the effective leak conductance  $g_L$  can in fact be negative.

Figs. 3A and 3B show that, as  $\gamma_L$  decreases, both  $Z_{max}$  and  $Z(0)$  increase, and so does  $Q_Z$  due to the different rates at which  $Z_{max}$  and  $Z(0)$  change in parameter space (Fig. 3D; see also Fig. 2D). The amplification of the voltage response is more dramatic for values of  $\gamma_L$  close to the boundary between the stability and instability regions, and is more pronounced for larger values of  $\gamma_1$ . In addition to these changes,  $\Lambda_{1/2}$  decreases with  $\gamma_L$ ; i.e., as  $\gamma_L$  decreases, the impedance profile becomes narrower and the selectivity increases (Figs. 3E and 3G). For values of  $\gamma_1$  close to the resonance curve, for which  $Z_{max}$  and  $Z(0)$  are not significantly different, resonance can be abolished for larger values of  $\gamma_L$  (see Fig. 2D).

Together, these results show that a decrease in  $\gamma_L$  (and therefore  $g_L$ ) causes an amplification of resonance, marked by an increase in the resonance amplitude  $Q_Z$  and an increase in the selectivity (decrease in  $\Lambda_{1/2}$ ), accompanied by a decrease in  $f_{res}$ . An increase in  $g_L$ , therefore, causes an attenuation of resonance accompanied by an increase in  $f_{res}$ .

**Resonance and oscillations**—To explore the distinction between membrane resonance and oscillations in the 2D linear model (i.e., the presence of a focus fixed point), we plotted the resonance and natural oscillation frequencies in the  $\gamma_L - \gamma_1$  parameter space (Fig. 4). A frequency of 0 indicates lack of oscillation or resonance, as indicated. We found that both  $f_{nat}$  and  $f_{res}$  increase with  $\gamma_1$  but do not generally coincide (see, for example, FIG. 4C). As  $\gamma_L$  is increased, both  $f_{nat}$  and  $f_{res}$  increase for small  $\gamma_L$  values but only  $f_{res}$  continues to increase with large  $\gamma_L$  values whereas  $f_{nat}$  decreases back to 0 in this range (Fig. 4D). Note that if  $\gamma_1$

is large (e.g.,  $\gamma_1 = 1$  here),  $f_{res}$  and  $f_{nat}$  almost coincide during the increasing part of  $f_{nat}$  as  $\gamma_L$  increases (not shown).

**An increase in  $g_1$  generates zero-phase-frequency with  $f_{phase} \neq f_{res}$** —We examined how the response phase of the membrane potential shifts with respect to the sinusoidal input current for the 2D linear system (6) with  $\tau_1 = 1$  and under what conditions the system exhibits zero-phase-frequency. For  $\gamma_1 = 0$  (low-pass filter), the phase  $\phi$  is always positive with  $\phi_{min} = \phi(0) = 0$  and the system does not exhibit zero-phase-frequency. Fig. 5A shows that this persists for values of  $\gamma_1 < 1$  for which the 2D system exhibits resonance but not zero-phase-frequency. For  $\gamma_1 > 1$ , a negative frequency band of length  $f_{phase}$  emerges (see also Fig. 5C). This band starts at  $f$  just above zero and its width also determines the zero-phase-frequency ( $= f_{phase}$ ). The value of  $f_{phase}$  increases with  $\gamma_1$  but is independent of  $\gamma_L$ . It should be noted that  $f_{phase}$  is different from the resonant frequency  $f_{res}$ , and the two variables have different monotonic dependencies on  $\gamma_1$ . Note also that the minimum phase  $\phi_{min}$  increases with  $\gamma_1$ , and therefore with  $f_{phase}$ , but decreases with  $\gamma_L$  (Fig. 5B).

**The effect of the time constant  $\tau_1$  on resonance**—We now consider the effect of the time constant  $\tau_1$  of the gating variable  $w_1$  (Eq. (6)). Although Figs. 2 to 5 were produced with  $\tau_1 = 1$ , the effects of changes in  $\tau_1$  can be investigated using these figures and Eqs. (14). When  $\tau_1 \neq 1$ , the normalized parameters are changed and therefore  $\gamma_L \neq g_L$  and  $\gamma_1 \neq g_1$ . For fixed values of  $g_L$  and  $g_1$ , changes in  $\tau_1$  cause  $\gamma_L$  and  $\gamma_1$  to move in parameter space along lines (parametrized by  $\tau_1$ ) with slopes  $\gamma_1/\gamma_L = g_1/g_L$  as shown in Fig. 6A. Each of these lines converges to the origin as  $\tau_1$  approaches zero, and its slope has the same sign as  $g_L$  (in the region of resonance for which  $g_1 > 0$ ). Fig. 6A shows that, for small enough values of  $\tau_1$ , the system exhibits neither intrinsic (damped) oscillations nor resonance, reflecting the fact that both phenomena depend upon a (relatively) slow negative feedback.

As  $\tau_1$  increases, the system exhibits first intrinsic oscillations with no resonance for small  $\tau_1$  and then, for larger values of  $\tau_1$ , both intrinsic oscillations and resonance (Figs. 6B1–B3; most clearly seen in 6B2). Depending on the slope  $\gamma_1/\gamma_L$ , intrinsic oscillations may disappear as  $\tau_1$  increases further. Note that for  $g_L < 0$ , relatively small increases in  $\tau_1$  causes the system to reach the instability region in parameter space.

An increase in  $\tau_1$  amplifies the voltage response and this amplification is marked by an increase in  $Q_z$  and  $Z_{max}$  (while  $Z(0)$  remains constant; Fig. 6C1–C3) and a decrease in  $\Lambda_{1/2}$  (i.e., increase in selectivity; not shown). The mechanism of generation of resonance as  $\tau_1$  increases is different from the mechanism described above for increasing values of  $g_1$  (with constant  $\tau_1$ ). Direct substitution of the model parameters ( $g_L$ ,  $g_1$  and  $\tau_1$ ) into Eq. (21) in Appendix A yields  $Z(0) = (g_L + g_1)^{-1}$ . In other words, changes in  $\tau_1$  do not affect the value of  $Z(0)$  and hence  $Q_z = Z_{max}$  for all values of  $\tau_1$ . As such, an increase in the time constant  $\tau_1$  generates resonance by an increase in  $Z_{max}$  with no changes in  $Z(0)$  (Fig. 6C1–3).

Increasing the time constant  $\tau_1$  causes the natural and resonant frequencies to increase for small values of  $\tau_1$  and to decrease for larger values. Information about the effect of  $\tau_1$  on the resonant and natural frequencies can, in principle, be extracted from Figs. 6B and 6C and the expressions for  $r_{1,2}$  and  $f_{res}$  in Eqs. (14). However, in most cases, especially when  $f_{nat}$  or  $f_{res}$

increase along lines in parameter space, the net effect of increasing values of  $\tau_1$  is not readily apparent from the graphs because both the numerator and denominator are increasing functions of  $\tau_1$ . In these cases, it is more useful to analyze the expressions  $f_{nat}$  and  $f_{res}$  given by Eqs. (19) and (22) in Appendix A. Substituting  $a = -g_L$ ,  $b = -g_1$ ,  $c = \tau_1^{-1}$ , and  $d = -\tau_1^{-1}$  yields

$$f_{nat} = \frac{1000}{2\pi} \frac{\sqrt{4g_1\tau_1 - (1 - g_L\tau_1)^2}}{2\tau_1} \quad f_{res} = \frac{1000}{2\pi} \frac{\sqrt{-1 + \sqrt{g_1^2\tau_1^2 + 2g_Lg_1\tau_1^2 + 2g_1\tau_1}}}{\tau_1} \quad (15)$$

Equation (15) gives the imaginary part of the eigenvalues (18) and is valid for calculating  $f_{nat}$  so long as the eigenvalues are complex. As such,  $f_{nat}$  is zero for the minimum value of  $\tau_1$  for which it is defined, reaches a maximum at  $\tau_1 = (2g_1 + g_L)^{-1}$  (provided this value is positive) and is zero again for large enough  $\tau_1$  when the right hand side of (15) fails to be a real number.  $f_{res}$  is zero for the minimum value of  $\tau_1$  for which it is defined

( $\tau_1 = (-g_1 + \sqrt{2g_1^2 + 2g_Lg_1}) / (g_1^2 + 2g_Lg_1)$ ), it is positive for larger values of  $\tau_1$  (e.g.,  $\tau_1 = g_1^{-1}$ ), and approaches zero as  $\tau_1$  approaches infinity (Figs. 6B1–3).

The non-monotonic effect of  $\tau_1$  on  $f_{res}$  is particularly clear in the impedance profile shown in Fig. 6C2. Note, however, that increasing  $\tau_1$  always results in an increase of the peak impedance value as seen in Fig. 6C1–3.

We now examine the effect of the time constant  $\tau_1$  on phase. Increasing  $\tau_1$  generates zero-phase-frequency with  $f_{phase} \neq f_{res}$ . As before, it is useful to examine the expression for  $\phi$  given by Eq. (23) in Appendix A. The zero-phase-frequency is obtained when the denominator in Eq. (23) vanishes. Substituting  $a = -g_L$ ,  $b = -g_1$ ,  $c = \tau_1^{-1}$ , and  $d = -\tau_1^{-1}$  yields

$$f_{phase} = \frac{1000}{2\pi} \frac{\sqrt{g_1\tau_1 - 1}}{\tau_1} \quad (16)$$

Zero-phase-frequency occurs for values of time constant  $\tau_1$  above  $g_1^{-1}$  as illustrated in Fig. 6D. Figs. 6D and 6C also illustrate that the critical value of  $\tau_1$  above which zero-phase-frequency occurs is different from the critical value above which resonance occurs. From Eq. (16), the zero-phase-frequency  $f_{phase}$  increases with  $\tau_1$  for  $\tau_1 < 2g_1^{-1}$  and decreases for larger values of  $\tau_1$ . A comparison between Eq. (16) and the second equation in (15) shows that in general  $f_{phase} \neq f_{res}$ .

## 2. Generation of resonance and zero-phase-frequency in linearized biophysical two-dimensional models

The study of the roles of the effective conductances  $g_1$  and  $g_L$  (or their dimensionless versions  $\gamma_1$  and  $\gamma_L$ ) on the generation of both resonance and zero-phase-frequency using the diagrams in Figs. 2 to 7 provides a mechanistic insight into these phenomena. However, it does not produce a useful explanation of the mechanisms underlying resonance and zero-

phase-frequency in realistic biophysical models. In this section we will use the description of the dependence of resonance and zero-phase-frequency in the 2D linear system, developed thus far, to explain how linear approximations to biophysical models can be mapped onto our framework of the linear systems and how biophysical ionic currents shape preferred frequencies for impedance and phase.

In the previous sections we kept one parameter fixed and varied another. Changes in either  $g_L$  or  $g_1$  resulted in trajectories in the  $g_L - g_1$  parameter space that moved along horizontal and vertical lines (Figs. 3–5). Additionally, changes in  $\tau_1$  generated oblique linear trajectories (Fig. 6). In contrast to these parameters, changes in the biophysical conductances may lead to nonlinear trajectories in the  $g_L - g_1$  parameter space. While changes in the biophysical leak ( $G_L$ ) and fast conductance ( $G_{x2}$ ) directly affect only the effective leak conductance  $g_L$  (Eq. (7)), changes in the biophysical conductances with slower time scales ( $G_{x1}$ ) affect both  $g_L$  and  $g_1$ . It is important to note, however, that changing  $G_L$  (or the fast conductances) may change the value of  $g_1$  indirectly, by changing the position of the fixed point.

In this section we investigate the effects of changes in the resonant and amplifying currents on the mechanisms of generation of resonance and zero-phase-frequency in two prototypical biophysical models  $I_h + I_p$  and  $I_{Ks} + I_p$ . The governing equations are given in Appendix B. The nonspecific cation  $h$  current  $I_h$  is a hyperpolarization-activated inward current whereas the slow non-inactivating potassium current (e.g., the M current)  $I_{Ks}$  is a depolarization-activated outward current and, as such, both  $I_h$  and  $I_{Ks}$  are resonant currents (Hutcheon and Yarom 2000). The depolarization-activated persistent sodium current  $I_p$  is an amplifying current (Hutcheon and Yarom 2000). The fact that  $I_h$  and  $I_{Ks}$  activate by moving the membrane potential in different directions (hyper- or depolarizing) results in qualitatively different effects on resonance and zero-phase-frequency properties, and their dependence on the biophysical conductances. These two models were chosen as representative models that are known to produce resonance but the effects of these ionic currents can be replaced by other currents with similar biophysical properties. The inward rectifying potassium currents can also act as amplifying currents; however, these currents are typically active in ranges of voltage below values where subthreshold resonance is observed and we do not examine their effect.

An increase in the maximal conductance of  $I_p$  generates strong nonlinearities in the  $I_h + I_p$  and  $I_{Ks} + I_p$  models as seen in the nullclines (Fig. 7). In the absence of  $I_p$  the nullclines are only weakly nonlinear; i.e., the linearized nullclines around the fixed-point  $V$  (the intersection between nullclines) provide a good approximation to the nonlinear nullclines. This is true in both models for a large range of values of  $V$ . An increase in the amount of  $I_p$  generates a strong nonlinearity (of parabolic type) in both models (Figs. 7A2 and 7B2). If the fixed-point  $V$  is near the “knee” of the  $V$ -nullcline, the linearized nullclines do not provide a good approximation to the nonlinear ones, and cannot be expected to capture the dynamics of the nonlinear system. For values of  $G_h$  and  $G_q$  for which  $V$  lies further away from the knee, however, along the left branch of the corresponding parabolic-like  $V$ -nullclines, the nullclines are only weakly nonlinear (not shown). Qualitatively, the phase plane diagrams for the two models are almost mirror images of each other (Fig. 7A vs. 7B).

Although an increase in  $G_h$  causes  $\bar{V}$  to increase while an increase in  $G_q$  causes  $\bar{V}$  to decrease, both phase planes respond in a similar way to changes in  $G_p$ .

**Nonlinear effects generated by increases in the maximal conductance of  $I_p$  are captured by the impedance profiles**—

Changes in the biophysical ionic conductances ( $G_h$ ,  $G_q$ , and  $G_p$ ) cause changes in the effective conductances  $g_L$  and  $g_1$  through Eqs. (7) and (8), and generate trajectories in  $\gamma_L - \gamma_1$  parameter space (Figs. 8A and 9A). The shapes of the trajectories in  $\gamma_L - \gamma_1$  parameter space depend not only on the biophysical conductances but also on the value of the fixed-point  $\bar{V}$  which, in turn, depends on the shape of the  $V$ -nullclines. Note that, for linear systems, the location of the fixed-point has no effect on the resonance and zero-phase-frequency properties. The nonlinearities of the  $V$ -nullclines are translated to the nonlinear trajectories in  $\gamma_L - \gamma_1$  parameter space through  $\bar{V}$ . If changes in  $G_h$ ,  $G_p$  and  $G_q$  had no effect on the location of  $\bar{V}$ , then an increase in  $G_p$  would still cause a decrease in the effective conductance  $g_L$ , and an increase in either  $G_h$  or  $G_q$  would cause an increase in both effective conductances  $g_L$  and  $g_1$ . In this case, changes in  $G_h$  and  $G_q$  would have generated oblique linear trajectories in  $\gamma_L - \gamma_1$  parameter space. If the changes in  $\bar{V}$  (as a result of changes in the biophysical conductances) are small, as it occurs when the nullclines are weakly nonlinear, then one would expect trajectories in parameter space to be weakly nonlinear as well, as is the case for the solid trajectories for  $G_p = 0$  (Figs. 8A and 9A). For larger values of  $G_p$  for which the nullclines are strongly nonlinear, the corresponding trajectories are also strongly nonlinear (dashed trajectories for  $G_p = 0.5$  in Figs. 8A and 9A).

**The effect of changing  $G_L$  in the biophysical models**—Our results in the dimensionless model indicated that increasing  $\gamma_L$  (and therefore  $g_L$ ) led to an increase in  $f_{res}$  (Fig. 4D). This raises the question of whether an increase in  $G_L$  in the biophysical models would also lead to a similar change in  $f_{res}$ . To examine this question, we varied the level of  $G_L$  in both the  $I_h + I_p$  and  $I_{Ks} + I_p$  models (Fig. 10). We found that, in both models, an increase in  $G_L$  led to a relatively small but noticeable increase in  $f_{res}$  (Figs. 10A1 and 10B1). The effect of  $G_L$  on  $f_{res}$  was not influenced much by the presence of  $I_p$  (i.e.  $0.5 G_p = 0.5$ ; Figs. 10A2 and 10B2).

**Changes in the maximal conductances of the resonant currents  $I_h$  and  $I_{Ks}$  in the presence of  $I_p$  have qualitatively different effects on the resonance and zero-phase-frequency**—

Resonant currents, or resonant gating variables, are usually classified into one single group (Richardson et al. 2003; Hutcheon and Yarom 2000). In the absence of  $I_p$ , changes in  $G_h$  and  $G_q$  generate weakly linear, almost oblique trajectories with positive slope in the corresponding  $\gamma_L - \gamma_1$  parameter spaces (solid arrowed curves in Figs. 8A and 9A). In this case, changes in  $G_h$  and  $G_q$  have similar effect on the resonance and zero-phase-frequency properties of the corresponding models.

In contrast, when  $I_p$  is present, changes in  $G_h$  and  $G_q$  affect the shape of the corresponding trajectories in almost opposite ways (Figs. 8A and 9A, dashed curves for  $G_p = 0.5$ ) reflecting the different biophysical roles these two currents play. In the  $I_h + I_p$  model, in particular, the direction of motion of the trajectories for  $G_p = 0.5$  and  $G_p = 0$  are opposite as  $G_h$  increases

and, for large enough values of  $\tau_1$ , trajectories cross the line  $\gamma_L = 0$  leading to a strong amplification of the voltage response (Fig. 8B2). This is in contrast to the  $I_{Ks} + I_p$  model where an increase in  $G_q$  leads to a strong de-amplification of the voltage response (Fig. 9B2). The differences between the trajectories in parameter space for the two models indicates that the dependence of their resonant properties on  $G_h$  or  $G_q$  are different. In particular,

- i. the voltage response is amplified for the  $I_h + I_p$  model and attenuated for the  $I_{Ks} + I_p$  model,
- ii. the selectivity increases ( $\Lambda_{1/2}$  decreases) for the  $I_h + I_p$  model and decreases ( $\Lambda_{1/2}$  increases) for the  $I_{Ks} + I_p$  model, and
- iii.  $\phi_{\min}$  increases in absolute value for the  $I_h + I_p$  model and decreases for the  $I_{Ks} + I_p$  model.

An increase in  $G_h$  reduces the voltage response for  $G_p = 0$  (Fig. 8B1) but amplifies the voltage response for  $G_p = 0.5$  (Fig. 8B2). This amplification is much stronger for larger values of  $I_{app}$  (not shown). In contrast, an increase in  $G_q$  reduces the voltage response for all values of  $G_p$  (Figs. 9B1 and 9B2). The amplification of the voltage response is still larger for larger values of  $I_{app}$  but this amplification is stronger for lower values of  $G_q$  (not shown).

In the  $I_h + I_p$  model both  $f_{res}$  and  $f_{phase}$  increase with increasing values of  $G_h$  but  $f_{res}$  decreases for high values of both  $G_h$  and  $G_p$ . For  $G_p = 0$ , both  $f_{res}$  and  $f_{phase}$  increase as  $G_h$  increases (Fig. 11A1; also see Figs. 8B1 and 8C1), and they do so almost linearly once resonance has been generated. In contrast, for  $G_p = 0.5$ , while  $f_{phase}$  increases with increasing values of  $G_h$ ,  $f_{res}$  first increases and then decreases (Fig. 11A1). These values of  $G_h$  and  $G_p$  correspond to a fixed-point located near the knee of the  $V$ -nullcline (Fig. 7A2). The switch in the monotonic behavior of  $f_{res}$  can therefore be attributed to a nonlinear effect.

In the  $I_{Ks} + I_p$  model  $f_{res}$  and  $f_{phase}$  increase with increasing values of  $G_q$  (Fig. 10B1; also see Figs. 9B1 and 9C1). This is similar to the increase of  $f_{res}$  and  $f_{phase}$  with  $G_h$  in the  $I_h + I_p$  model (Fig. 11A1). Note however that, in contrast to the  $I_h + I_p$  model,  $f_{phase}$  is larger for  $G_p = 0.5$  than for  $G_p = 0$ , and  $f_{res}$  is almost insensitive to changes in  $G_p$  (Fig. 11B1). For  $G_p = 0$  neither model show intrinsic oscillatory activity, but oscillatory activity can emerge for  $G_p > 0$  and with  $G_h$  above a certain threshold (Fig. 11A1) or  $G_q$  below a certain threshold (Fig. 11B1; also see Figs. 11A2 and 11B2). Interestingly, as  $G_h$  increases,  $f_{res}$  decreases and  $f_{nat}$  increases and these frequencies approach the same value (Fig. 11A1). Similarly, the values of  $f_{res}$  and  $f_{nat}$  approach the same value but, in contrast to the  $I_h + I_p$  model, as  $G_q$  decreases ( $I_{Ks} + I_p$  model; Fig. 11B1). The fact that the nullclines of the two models are qualitatively mirror images of each other suggests that for these parameter values both models might have a common underlying mechanism for the generation of both intrinsic oscillations and resonance.

Similarly, in the  $I_h + I_p$  and  $I_{Ks} + I_p$  models  $Z_{max}$  and  $Q_Z$  show opposite monotonic behaviors as  $G_h$  and  $G_q$  increase for  $G_p > 0$ . Even though, in both models, when  $G_p = 0$ ,  $Z_{max}$  and  $Q_Z$  are small and almost insensitive to changes in  $G_h$  and  $G_q$  (Figs. 11A3 and 11B3), when  $G_p > 0$ , these models exhibit opposite behaviors as the corresponding resonant



conductance increases : in the  $I_h + I_p$  model resonance is amplified by increasing  $G_h$  while in the  $I_{Ks} + I_p$  model resonance is attenuated by increasing  $G_q$  (Figs. 11A3 and 11B3). Note that the largest values of both  $Z_{max}$  and  $Q_Z$  occur in the strongly nonlinear regions in parameter space referred to above. The increase in  $Q_Z$  and decrease in  $Z_{max}$  as  $G_h$  and  $G_q$  demonstrate that, in both models, resonance is created by a combined decrease in both  $Z_{max}$  and  $Z(0)$  as explained in the previous section for the reduced models.

We now turn to the effect of  $G_p$  in the two models.  $f_{res}$  has a similar monotonic behavior as  $G_p$  changes in the two models but  $f_{phase}$  has a different monotonic behavior as  $G_p$  changes in the two models. Figs. 11A2 and 11B2 show the behavior of both  $f_{res}$  and  $f_{phase}$  as  $G_p$  increases. In both models,  $f_{res}$  decreases with increasing values of  $G_p$ . This change is more pronounced in the  $I_h + I_p$  model than in the  $I_{Ks} + I_p$  model. The dependence of  $f_{phase}$  with  $G_p$  is different in the two models:  $f_{phase}$  slightly decreases in the former and increases in the latter. Interestingly, in spite of the different monotonic behavior between the two models, the difference between  $f_{res}$  and  $f_{phase}$  decreases as  $G_p$  increases, and both characteristic frequencies become closer in the nonlinear region in parameter space with a high amplifying effect (Figs. 11A2 and 11B2). As mentioned above, neither model shows intrinsic oscillations for low values of  $G_p$  but oscillations arise as  $G_p$  increases (Figs. 11A2 and 11B2).

The amplification of the voltage response due to increasing values of  $G_p$  dramatically increases in the nonlinear region in parameter space in the two models. This is seen in Figs. 11A4 and 11B4 (see also Figs. 8 and 9) where both  $Z_{max}$  and  $Q_Z$  increase for large values of  $G_p$  as either  $G_h$  increases) or  $G_q$  decreases. This amplification does not occur for  $G_p = 0$  or with  $G_p = 0.5$  together with lower values of  $G_h$  or larger values of  $G_q$ , suggesting that it results from the strong nonlinearities present in both models for large values of  $G_p$ .

**$f_{res}$  and  $f_{phase}$  decrease with increasing values of the time constant  $\tau_1$  in the two models**—For the  $I_h + I_p$  model (Fig. 12A1),  $f_{res}$  and  $f_{phase}$  are both decreasing functions of  $\tau_1$ , and are both larger for  $G_p = 0$  than for  $G_p > 0$ . For  $G_p > 0$ , the difference between  $f_{res}$  and  $f_{phase}$  decreases and they approach identical values. For the  $I_{Ks} + I_p$  model (Fig. 12B2),  $f_{phase}$  first increases with  $\tau_1$  for  $G_p = 0$  and then decreases. For  $G_p = 0.5$ , both  $f_{res}$  and  $f_{phase}$  are decreasing functions of  $\tau_1$ . In contrast to the  $I_h + I_p$  model, in the  $I_{Ks} + I_p$  model,  $f_{res}$  and  $f_{phase}$  are larger for  $G_p > 0$  than for  $G_p = 0$ , although the difference between  $f_{res}$  for these two values of  $G_p$  is very small.

The two models show also similarities and differences in their natural frequencies as a function of  $\tau_1$ . As mentioned above, neither model shows intrinsic oscillations for  $G_p = 0$ . For  $G_p > 0$ , in both models  $f_{res}$  is always larger than  $f_{nat}$  (Figs. 12A1 and 12B1). For the  $I_h + I_p$  model (Fig. 12A1),  $f_{res}$  and  $f_{nat}$  are almost identical for all values of  $\tau_1$  (and  $G_p > 0$ ), while the value of  $f_{res}$  is significantly different than for  $G_p = 0$ . In contrast, for the  $I_{Ks} + I_p$  model (Fig. 12B1), intrinsic oscillations (for  $G_p > 0$ ) disappear as  $\tau_1$  increases and  $f_{res}$  is not significantly different for different values of  $G_p$ .

Resonance is amplified as  $\tau_1$  increases in the presence of  $I_p$  in the two models. In the absence of  $I_p$  ( $G_p = 0$ ) both  $Z_{max}$  and  $Q_Z$  are insensitive to changes in the time constant  $\tau_1$



(Figs. 12A2 and 12B2). However, for  $G_p = 0.5$ , both  $Z_{max}$  and  $Q_Z$  increase as  $\tau_1$  increases. Their difference remains constant since changes in  $\tau_1$  have no effect on  $Z(0)$ . Note that changes in  $Z_{max}$  and  $Q_Z$  with  $\tau_1$  are more pronounced for the  $I_h + I_p$  model (Fig. 12A2) than for the  $I_{Ks} + I_p$  model (Fig. 12B2).

Finally, although for the sake of brevity we do not show these data,  $f_{res}$  and  $f_{phase}$  are almost insensitive to changes in  $I_{app}$  in the two models whereas resonance ( $Z_{max}$  and  $Q_Z$ ) is significantly amplified by increasing values of  $I_{app}$  in the presence of  $I_p$  in both models.

## Discussion

A large number of studies in recent years has focused on subthreshold membrane resonance in neurons, its dependence on ionic currents and its influence on neuronal and network oscillations (Richardson et al. 2003; Ledoux and N. 2011; Castro-Alamancos et al. 2007; Tohidi and Nadim 2009; Izhikevich et al. 2003; Engel et al. 2008; Reinker et al. 2004; Kispersky et al. 2012; Moca et al. 2012; Thevenin et al. 2011). Subthreshold membrane resonance is primarily described on the basis of a linear *RLC* circuit where  $R$  is equated with the membrane resistance,  $C$  with the membrane capacitance and the inductance  $L$ , more abstractly, with voltage-gated ionic conductance properties (Erchova et al. 2004). Membrane resonance is defined by a peak in the impedance amplitude plotted as a function of input frequency (the impedance profile) and can be characterized by a few attributes describing this impedance profile (Fig. 1B1). The frequency and quality (“peakiness”) of membrane resonance is captured by these attributes. A number of voltage-gated ionic currents are known to result in membrane resonance. Yet, even in a simple model neuron that is based on biophysical currents, the dependence of the attributes of the impedance profile on biophysical parameters such as the maximal conductances of the leak and voltage-gated currents is neither well-described nor intuitive.

In the first part of this paper we used a linear 2D model (Richardson et al. 2003) to show how the attributes of the resonance and phase profiles depend on three model parameters, the two effective conductances and the time constant. This analysis resulted in graphs that show how resonance and phase depend on the model parameters (Figs. 2–5). We also compared the resonance frequency in this model with the frequency of subthreshold oscillations, when present (Fig. 4). In the second part, we used this description to understand the emergence and properties of resonance and phase-frequency relationships in two representative conductance-based biophysical models. We began by exploring how changing a biophysical parameter affected the linearization (about an equilibrium point) of the conductance-based model. We then mapped the resulting trajectories (parameterized by the biophysical parameter) in the effective-conductance parameter space described in part one. These trajectories provided us with information on the dependence of resonance and phase attributes on the biophysical parameter. Together, these two parts provide a framework to study linear impedance and to analyze how changing biophysical parameters affects linear resonance and phase profiles in nonlinear conductance-based models. We limited our analysis to 2D models where the linear system is effectively described by two parameters and could be readily illustrated graphically. The framework we presented can be

readily generalized to higher-dimensional models by projecting to lower-dimensional parameter spaces or in the form of look-up tables.

We identified two qualitatively different mechanisms for the generation of resonance in 2D systems. The first mechanism depends on the effective conductance  $\gamma_1$ : as  $\gamma_1$  increases, there is a decrease in both  $Z_{max}$  and  $Z(0)$  but the latter decreases at a higher rate (Fig. 3C) which results in an increase in  $Q_Z$ . The second mechanism is due to changing  $\tau_1$ . For very small values of  $\tau_1$  the 2D system does not exhibit resonance (Fig. 6A). As  $\tau_1$  increases, the system first transitions through a region of the parameter space which shows intrinsic (damped) oscillations with no resonance and for larger values of  $\tau_1$  resonance emerges (Fig. 6A–B). Increasing  $\tau_1$  further can allow the system to resonance without subthreshold oscillations (Fig 6B1–B2). As such, factors such as temperature that modulate time constants can allow a neuron to transition to resonance without changing the maximal conductances of expressed ionic currents.

The phenomenon of subthreshold resonance is often related to the presence of subthreshold oscillations (Lampf and Yarom 1997) although it is known that these are separate phenomena even in linear models (Richardson et al. 2003). The analysis of the linear 2D model shows that in certain parameter ranges these two frequencies can show similar parameter dependence but that they are also clearly distinct (Fig. 4).

Typically the voltage response of a neuron is studied by focusing on the amplitude of the impedance profile (Hutcheon and Yarom 2000). Yet, just as the impedance amplitude describes the scaling of the membrane potential, the impedance phase as a function of frequency (the phase profile) describes the membrane potential phase shift in response to an oscillatory current. The zero-phase-frequency  $f_{phase}$ —the frequency at which the input current and the membrane potential are synchronous in phase—provides information complementary to the resonance frequency  $f_{max}$  (Richardson et al. 2003). Although in an *RLC* circuit in series the values of  $f_{phase}$  and  $f_{max}$  are equal, in parallel circuits, such as membrane equivalent circuits, the two values remain distinct (Fig. 1B). Here we examined the dependence of  $f_{phase}$  in a 2D system and found that this frequency remains independent of the effective leak conductance, although the extent to which negative phase shifts occur ( $\phi_{min}$ ) does change with both effective leak and voltage-gated conductances (Fig. 5).

The zero-phase-frequency  $f_{phase}$  has been measured experimentally for the subthreshold response (Gutfreund et al. 1995) or the spike phase response (Fuhrmann et al. 2002; Smith et al. 2000; Carandini et al. 1996). In the latter case,  $f_{phase}$  was used in network models of spiking neurons in determining population synchrony (Fuhrmann et al. 2002). Our analysis provides a description of the dependence of  $f_{phase}$  of the subthreshold linear response on model parameters. As the amplitude of the response approaches threshold, this dependence can be used as a first-order approximation for the neuron's spike phase and therefore provides a mechanistic understanding of how model ionic currents can affect spike phase.

Voltage-gated ionic conductances have been classified into resonant and amplifying (Hutcheon and Yarom 2000; Richardson et al. 2003) with the underlying implication that all currents in each group behave similarly with respect to changes in parameters. Here we

explored two representative conductance-based models with distinct resonant currents, one hyperpolarization-activated ( $I_h$ ) and the other depolarization-activated ( $I_{Ks}$ ). We found that, in the absence of an amplifying current ( $I_p$ ), the resonant attributes in both models exhibit a similar dependence on the conductance of the two respective resonant currents. This is most easily seen by comparing the solid trajectories in Figs. 8A, B1 and C1 with the corresponding panels of Fig. 9. In contrast, in the presence of the amplifying current  $I_p$ , changing the conductance of the resonant current in the two models has opposite effects on the attributes of resonance. For instance, whereas increasing  $G_h$  can amplify the voltage response, a similar increase in  $G_q$  does the opposite (Figs. 8B2 and 9B2). Similarly, increasing these two conductances in the respective models can have opposite effects on the properties of the phase profile (Figs. 8C2 and 9C2). The difference in the effects of  $G_h$  and  $G_q$  are again readily observed by examining the corresponding trajectories in the effective-conductance parameter space (compare dashed curves in Figs. 8A and 9A). Although these differences are expected, they have been previously overlooked in the analysis of membrane resonance in neural models.

One of the interesting results of the analysis of the dimensionless model is that an increase in the effective leak conductance  $g_L$  leads to an increase in the resonance frequency (Fig. 4D). Recent experimental results have indicated that manipulating the leak conductance does not change  $f_{res}$  significantly (Fernandez et al. 2013; Fernandez and White 2008). For comparison, we varied the levels of  $G_L$  in our 2D biophysical models and found that the changes in  $f_{res}$  were much smaller than those seen in Fig. 4D and, in some cases, almost unnoticeable (Fig. 10). This difference is due to two factors. First, a change in  $G_L$  in the biophysical model does not result in a linear (vertical) trajectory in the  $\gamma_L - \gamma_1$  parameter space. Second, the changes in the parameter values using the linear approximation cannot account for the nonlinear effects of the biological neurons or the biophysical models. A proper exploration of the effects of the leak conductance requires tracking the nonlinear properties of the neurons which is beyond the scope of the current study.

It is important to note that the effect of subthreshold preferred frequencies on the spiking activity of neurons is not straightforward. Although there is experimental evidence of the correlations between subthreshold resonance and spiking activity and, in some cases, this is supported by modeling (Richardson et al. 2003), the spike frequency of neurons is shaped by factors, such as refractoriness, that are nonlinear and are not restricted to the subthreshold regime (Broicher et al. 2012). In particular, the ability of a neuron or network to produce spiking or oscillations cannot be simply equated with how the neuron or network responds to inputs of different frequencies (Fernandez and White 2008; Stark et al. 2013).

In this study we have explored the properties of resonance and phase profiles in a linear system and used this information to examine similar properties for linearizations of simple conductance-based models. Interestingly, some effects of the nonlinearities in the models are captured by the nonlinear trajectories in the effective-conductance parameter space. Yet, it is important to note that the linearizations do not capture other effects that may arise due to nonlinearities that are present even in these simplified conductance-based models. Such effects include, but are not limited to, nonlinear amplifications of the voltage response with

input current and the emergence of voltage responses that do not match the input frequency. We will address these issues in future work.

## Acknowledgments

The authors thank Diana Martinez and David Fox for their comments on this manuscript.

Grants

Supported by NSF DMS0817241 (HGR) and NIH MH060605 (FN).

## Appendix A. Two-dimensional linear systems: eigenvalues, natural frequency and impedance

Consider the following two-dimensional linear system

$$\begin{cases} X' = aX + bY + A_{in}e^{i\omega t} \\ Y' = cX + dY \end{cases} \quad (17)$$

$a$ ,  $b$ ,  $c$  and  $d$  are constant,  $\omega > 0$  and  $A_{in} \geq 0$ .

### Intrinsic oscillations and natural frequency

The Jacobian of the corresponding homogeneous system ( $A_{in} = 0$ ) is given by

$$J = \begin{pmatrix} a & b \\ c & d \end{pmatrix}.$$

The roots of the characteristic polynomial are given by

$$r_{1,2} = \frac{(a+d) \pm \sqrt{(a-d)^2 + 4bc}}{2}. \quad (18)$$

From Eq. (18), the homogeneous system displays stable oscillatory solutions (focus points) for values of the parameters satisfying

$$(a-d)^2 + 4bc < 0 \quad a+d \leq 0.$$

The natural frequency is given by

$$\mu = \frac{\sqrt{4bc + (a-d)^2}}{2}. \quad (19)$$

### Impedance function

The particular solutions to system (17) have the form

$$X_p(t) = A_{out} e^{i\omega t} \quad Y_p(t) = B_{out} e^{i\omega t}$$

Substituting into system (17) and rearranging terms we obtain

$$\begin{pmatrix} i\omega - a & -b \\ -c & i\omega - d \end{pmatrix} \begin{pmatrix} A_{out} \\ B_{out} \end{pmatrix} = \begin{pmatrix} A_{in} \\ 0 \end{pmatrix}. \quad (20)$$

By solving the algebraic system (20) we obtain

$$Z(\omega) = \frac{A_{out}}{A_{in}} = \frac{-d + i\omega}{(ad - bc - \omega^2) - i\omega(a+d)}, \quad |Z(\omega)|^2 = \frac{A_{out}^2}{A_{in}^2} = \frac{d^2 + \omega^2}{(ad - bc - \omega^2)^2 + (a+d)^2 \omega^2}. \quad (21)$$

The impedance  $Z$  peaks at the resonant frequency

$$\omega_{res} = \sqrt{-d^2 + \sqrt{b^2 c^2 - 2abcd - 2d^2 bc}}. \quad (22)$$

The impedance phase is given by

$$\tan(\phi) = \frac{(ad - bc - \omega^2)\omega - (a+d)\omega d}{(ad - bc - \omega^2)d + (a+d)\omega^2} = - \frac{bc + d^2 + \omega^2}{(ad - bc)d + a\omega^2} \omega. \quad (23)$$

## Appendix B. The 2D Biophysical Models

The voltage-dependent activation/inactivation curves  $x_\infty(V)$  and voltage-dependent time scales  $\tau_x(V)$  used in the kinetic Eq. (3) for the gating variables  $x$  are frequently expressed in terms of

$$x_\infty(V) = \frac{\alpha_x(V)}{\alpha_x(V) + \beta_x(V)} \quad \tau_x(V) = \frac{1}{\alpha_x(V) + \beta_x(V)}. \quad (24)$$

Below we present the functions and parameters corresponding to the various models we use in this paper.

### $I_h + I_p$ model

This model has been proposed in (Acker et al. 2003). It has a persistent sodium current and a two-component (fast and slow) h-current given by  $I_p = G_p p(V - E_{Na}) = G_p p_\infty(V)(V - E_{Na})$  and  $I_h = G_h r(V - E_h) = G_h(c_f r_f + c_s r_s)(V - E_h)$  respectively with  $E_h = -20$  mV,  $E_{Na} = 55$  mV,  $c_f = 0.65$  and  $c_s = 0.35$ . The voltage-dependent activation/inactivation and time constants are given by

$$\begin{aligned}
p_{\infty}(V) &= 1 / (1 + e^{-(V+38)/6.5}) \\
\tau_p(V) &= 0.15 \\
r_{f,\infty}(V) &= 1 / (1 + e^{(V+79.2)/9.78}) \\
\tau_{rf}(V) &= 0.51 / (e^{(V-1.7)/10} + e^{-(V+340)/52}) + 1 \\
r_{s,\infty}(V) &= 1 / (1 + e^{(V+71.3)/7.9}) \\
\tau_{rs}(V) &= 5.6 / (e^{(V-1.7)/14} + e^{-(V+260)/43}) + 1.
\end{aligned}$$

### $I_{Ks} + I_p$ model

This model has been proposed in (Acker et al. 2003). It has a persistent sodium current and a slow potassium (M-type) current given by  $I_p = G_p p(V - E_{Na}) = G_p p_{\infty}(V)(V - E_{Na})$  and  $I_{Ks} = G_q q(V - E_K)$  with  $E_{Na} = 55$  mV and  $E_K = -90$  mV. The voltage-dependent activation/inactivation and time constants are given by

$$p_{\infty}(V) = 1 / (1 + e^{-(V+38)/6.5}) \quad \tau_p(V) = 0.15 \quad q_{\infty}(V) = 1 / (1 + e^{-(V+35)/6.5}) \quad q_{\tau}(V) = 90$$

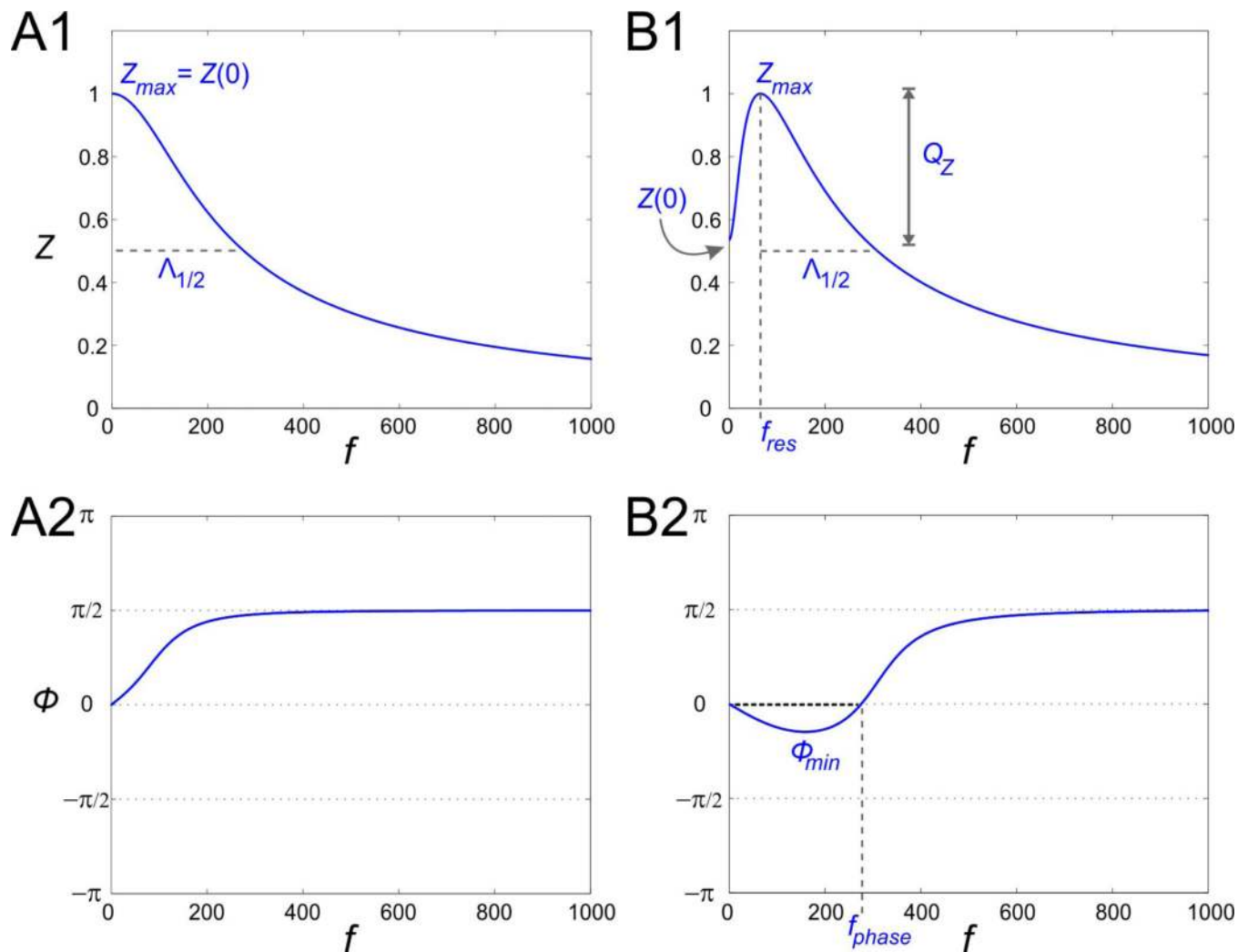
### References

- Acker CD, Kopell N, White JA. Synchronization of strongly coupled excitatory neurons: Relating network behavior to biophysics. *Journal of Computational Neuroscience*. 2003; 15:71–90. [PubMed: 12843696]
- Broicher T, Malerba P, Dorval AD, Borisyuk A, Fernandez FR, White JA. Spike phase locking in CA1 pyramidal neurons depends on background conductance and firing rate. *J. Neurosci*. 2012; 32:14374–14388. [PubMed: 23055508]
- Carandini M, Mechler F, Leonard CS, Movshon JA. Spike train encoding by regular-spiking cells of the visual cortex. *J. Neurophysiol*. 1996; 76:3425–3441. [PubMed: 8930283]
- Castro-Alamancos MA, Rigas P, Tawara-Hirata Y. Resonance (approximately 10 Hz) of excitatory networks in motor cortex: Effects of voltage-dependent ion channel blockers. *J Physiol*. 2007; 578:173–191. [PubMed: 16945964]
- Dembrow NC, Chitwood RA, Johnston D. Projection-specific neuromodulation of medial prefrontal cortex neurons. *J Neurosci*. 2010; 30(50):16922–16937. [PubMed: 21159963]
- Dickson CT, Alonso AA. Muscarinic induction of synchronous population activity in the entorhinal cortex. *J. Neurosci*. 1997; 17(7):6729–6744. [PubMed: 9254685]
- Engel TA, Schimansky-Geier L, Herz AV, Schreiber S, Erchova I. Subthreshold membrane-potential resonances shape spike-train patterns in the entorhinal cortex. *J. Neurophysiol*. 2008; 100:1576–1588. [PubMed: 18450582]
- Erchova I, Kreck G, Heinemann U, Herz AV. Dynamics of rat entorhinal cortex layer II and III cells: Characteristics of membrane potential resonance at rest predict oscillation properties near threshold. *J Physiol*. 2004; 560:89–110. [PubMed: 15272028]
- Ermentrout, GB.; Terman, D. *Mathematical Foundations of Neuroscience*. Springer; 2010.
- Fernandez FR, Malerba P, Bressloff PC, White JA. Entorhinal stellate cells show preferred spike phase-locking to theta inputs that is enhanced by correlations in synaptic activity. *J Neurosci*. 2013; 33(14):6027–6040. [PubMed: 23554484]
- Fernandez FR, White JA. Artificial synaptic conductances reduce subthreshold oscillations and periodic firing in stellate cells of the entorhinal cortex. *J. Neurosci*. 2008; 28:3790–3803. [PubMed: 18385337]

- Fuhrmann G, Markram H, Tsodyks M. Spike frequency adaptation and neocortical rhythms. *J Neurophysiol.* 2002; 88(2):761–770. [PubMed: 12163528]
- Gray CM. Synchronous oscillations in neuronal systems: mechanisms and functions. *J Comp Neuroscience.* 1994; 1:11–38.
- Gutfreund Y, Yarom Y, Segev I. Subthreshold oscillations and resonant frequency in guinea pig cortical neurons: Physiology and modeling. *J Physiol.* 1995; 483:621–640. [PubMed: 7776248]
- Haas JS, White JA. Frequency selectivity of layer II stellate cells in the medial entorhinal cortex. *J Neurophysiol.* 2002; 88:2422–2429. [PubMed: 12424283]
- Hodgkin AL, Huxley AF. A quantitative description of membrane current and its application to conductance and excitation in nerve. *J Physiol.* 1952; 117:500–544. [PubMed: 12991237]
- Hu H, Vervaeke K, Storm JF. Two forms of electrical resonance at theta frequencies generated by M-current, h-current and persistent Na<sup>+</sup> current in rat hippocampal pyramidal cells. *J Physiol.* 2002; 545.3:783–805. [PubMed: 12482886]
- Hutcheon B, Miura RM, Puil E. Subthreshold membrane resonance in neocortical neurons. *J Neurophysiol.* 1996; 76:683–697. [PubMed: 8871191]
- Hutcheon B, Yarom Y. Resonance oscillations and the intrinsic frequency preferences in neurons. *Trends Neurosci.* 2000; 23:216–222. [PubMed: 10782127]
- Izhikevich EM, Desay NS, Walcott EC, Hoppensteadt FC. Bursts as a unit of neural information: Selective communication via resonance. *Trends Neurosci.* 2003; 26:161–167. [PubMed: 12591219]
- Kispersky TJ, Fernandez FR, Economo MN, White JA. Spike resonance properties in hippocampal O-LM cells are dependent on refractory dynamics. *J. Neurosci.* 2012; 32:3637–3651. [PubMed: 22423087]
- Lampl I, Yarom Y. Subthreshold oscillations and resonant behaviour: Two manifestations of the same mechanism. *Neuron.* 1997; 78:325–341.
- Lau T, Zochowski M. The resonance frequency shift, pattern formation, and dynamical network reorganization via sub-threshold input. *PLoS ONE.* 2011; 6:e18983. [PubMed: 21526162]
- Ledoux E, N B. Dynamics of networks of excitatory and inhibitory neurons in response to time-dependent inputs. *Frontiers in Computational Neuroscience.* 2011; 5:1–17. [PubMed: 21267396]
- Llinás RR, Yarom Y. Oscillatory properties of guinea pig olivary neurons and their pharmacological modulation: An *in vitro* study. *J Physiol.* 1986; 376:163–182. [PubMed: 3795074]
- Marder E, Calabrese RL. Principles of rhythmic motor pattern generation. *Physiol. Rev.* 1996; 76:687–717. [PubMed: 8757786]
- Moca VV, Nicolic D, Singer W, Muresan R. Membrane resonance enables stable robust gamma oscillations. *Cerebral Cortex*, Epub ahead of print. 2012
- Morris C, Lecar H. Voltage oscillations in the barnacle giant muscle fiber. *Biophys. J.* 1981; 35:193–213. [PubMed: 7260316]
- Narayanan R, Johnston D. Long-term potentiation in rat Hippocampal neurons is accompanied by spatially widespread changes in intrinsic oscillatory dynamics and excitability. *Neuron.* 2007; 56:1061–1075. [PubMed: 18093527]
- Reboreda A, Sanchez E, Romero M, Lamas JA. Intrinsic spontaneous activity and subthreshold oscillations in neurones of the rat dorsal column nuclei in culture. *J Physiol.* 2003; 551(Pt 1):191–205. [PubMed: 12844503]
- Reinker S, Puil E, Miura RM. Membrane resonance and stochastic resonance modulate firing patterns of thalamocortical neurons. *Journal of Computational Neuroscience.* 2004; 16:15–25. [PubMed: 14707541]
- Richardson MJE, Brunel N, Hakim V. From subthreshold to firing-rate resonance. *J. Neurophysiol.* 2003; 89:2538–2554. [PubMed: 12611957]
- Rinzel, J.; Ermentrout, GB. Analysis of neural excitability and oscillations. In: Koch, C.; Segev, I., editors. *Methods in Neural Modeling*, second edition. Vol. 251. Cambridge, Massachusetts: MIT Press; 1998. p. 292

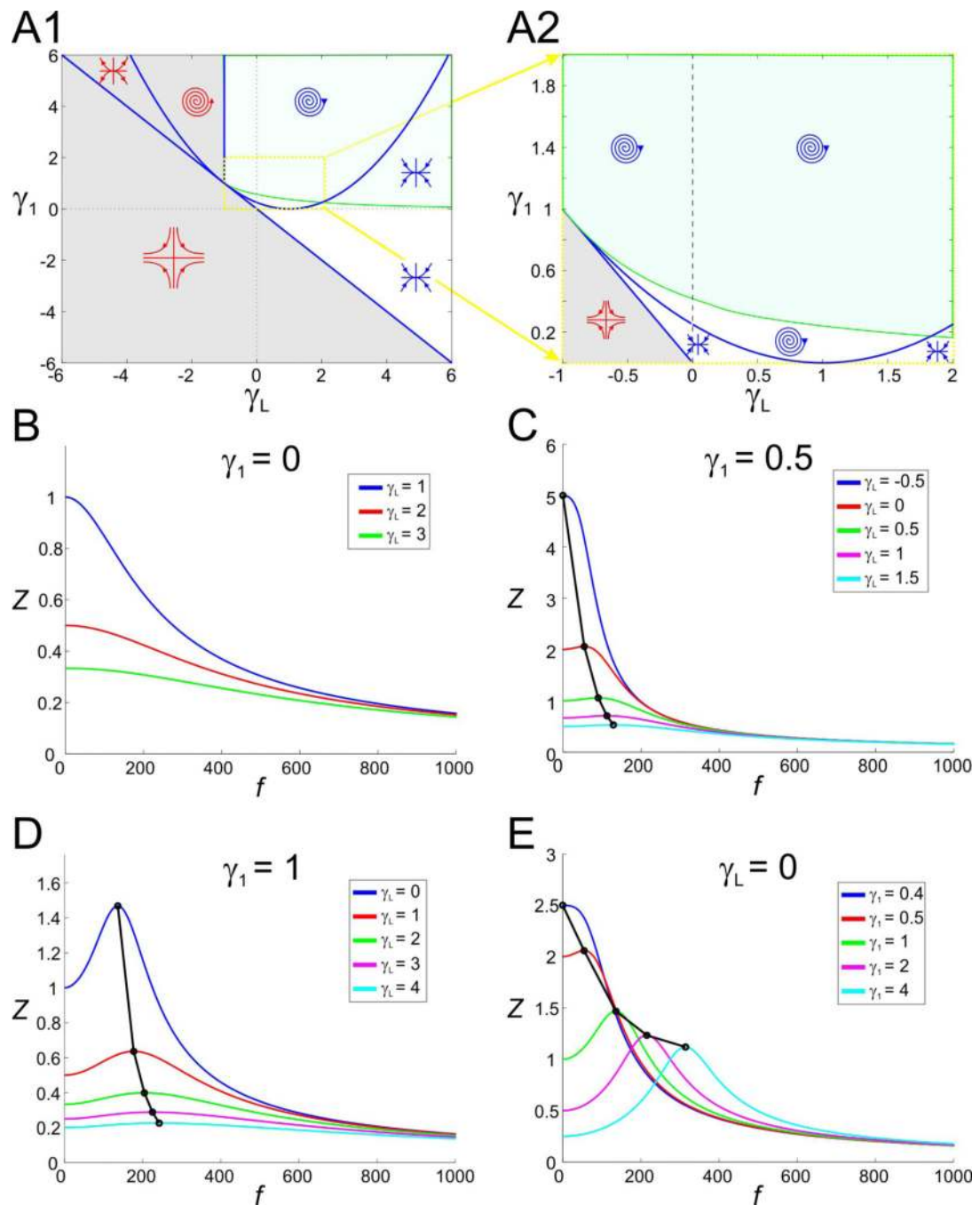


- Rotstein HG, Oppermann T, White JA, Kopell N. A reduced model for medial entorhinal cortex stellate cells: Subthreshold oscillations, spiking and synchronization. *Journal of Computational Neuroscience*. 2006; 21:271–292. [PubMed: 16927211]
- Schmitz D, Gloveli T, Behr J, Dugladze T, Heinemann U. Subthreshold membrane potential oscillations in neurons of deep layers of the entorhinal cortex. *Neuron*. 1998; 85:999–1004.
- Schreiber S, Erchova I, Heinemann U, Herz AV. Subthreshold resonance explains the frequency-dependent integration of periodic as well as random stimuli in the entorhinal cortex. *J. Neurophysiol*. 2004; 92:408–415. [PubMed: 15014100]
- Sciamanna G, Wilson CJ. The ionic mechanism of gamma resonance in rat striatal fast-spiking neurons. *J. Neurophysiol*. 2011; 106:2936–2949.
- Smith GD, Cox CL, Sherman SM, Rinzel J. Fourier analysis of sinusoidally driven thalamocortical relay neurons and a minimal integrate-and-fire-or-burst model. *J. Neurophysiol*. 2000; 83(1):588–610. [PubMed: 10634897]
- Stark E, Eichler R, Roux L, Fujisawa S, Rotstein HG, Buzsáki G. Inhibition-induced theta resonance in cortical circuits. *Neuron*. 2013 In Press.
- Thevenin J, Romanelli M, Vallet M, Brunel M, Erneux T. Resonance assisted synchronization of coupled-oscillators: frequency locking without phase locking. *Phys. Rev. Lett*. 2011;107–104101.
- Tohidi V, Nadim F. Membrane resonance in bursting pacemaker neurons of an oscillatory network is correlated with network frequency. *J. Neurosci*. 2009; 6427:6435.
- Wang XJ. Neurophysiological and computational principles of cortical rhythms in cognition. *Physiological Review*. 2010; 90:1195–1268.
- Wu N, Hsiao C-F, Chandler SH. Membrane Resonance and Subthreshold Membrane Oscillations in Mesencephalic V Neurons: Participants in Burst Generation. *J. Neurosci*. 2001; 21:3729–3739. [PubMed: 11356860]



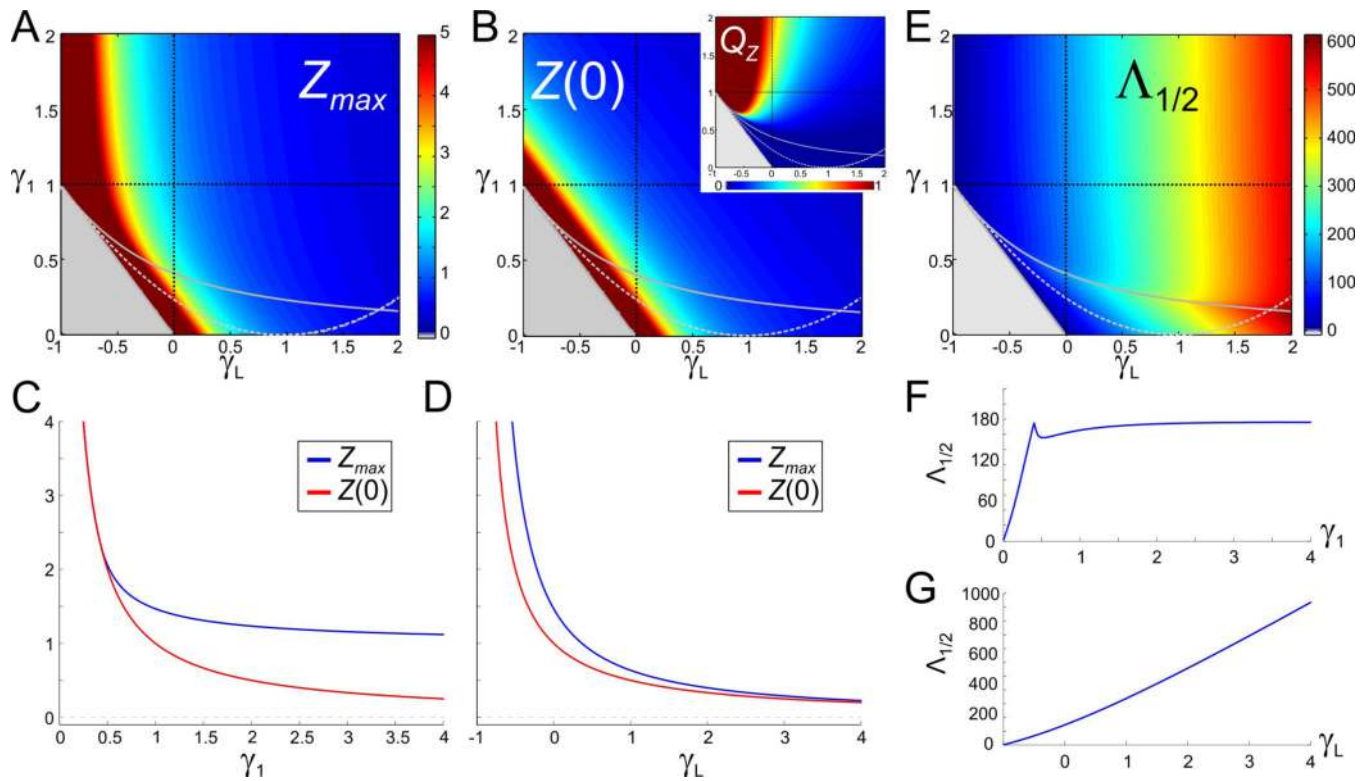
**Figure 1.**

Impedance ( $Z$ ) and phase ( $\phi$ ) profile diagrams. **A1.** The impedance profile of a low-pass filter RC cell. **A2.** The RC cell in A1 only shows a positive response phase. **B1.** The impedance profile of a band-pass filter resonant cell. The resonant frequency  $f_{res}$  is the frequency at which the impedance function reaches its maximum  $Z_{max}$ . The parameter  $Q_Z$  is defined as the difference between  $Z_{max}$  and  $Z_0$ . The characteristic frequency range  $\Lambda_{1/2}$  measures the length of the frequency interval for which  $Z(f)$  is above  $1/2$  of its maximum value. **B2.** The phase of the resonant cell shown in B1 includes both a negative and a positive region.  $\phi_{min}$  is the minimum phase and  $f_{phase}$  represents the zero-phase-frequency and is equal to the length of the frequency band for which the voltage response leads the input signal (negative phase).

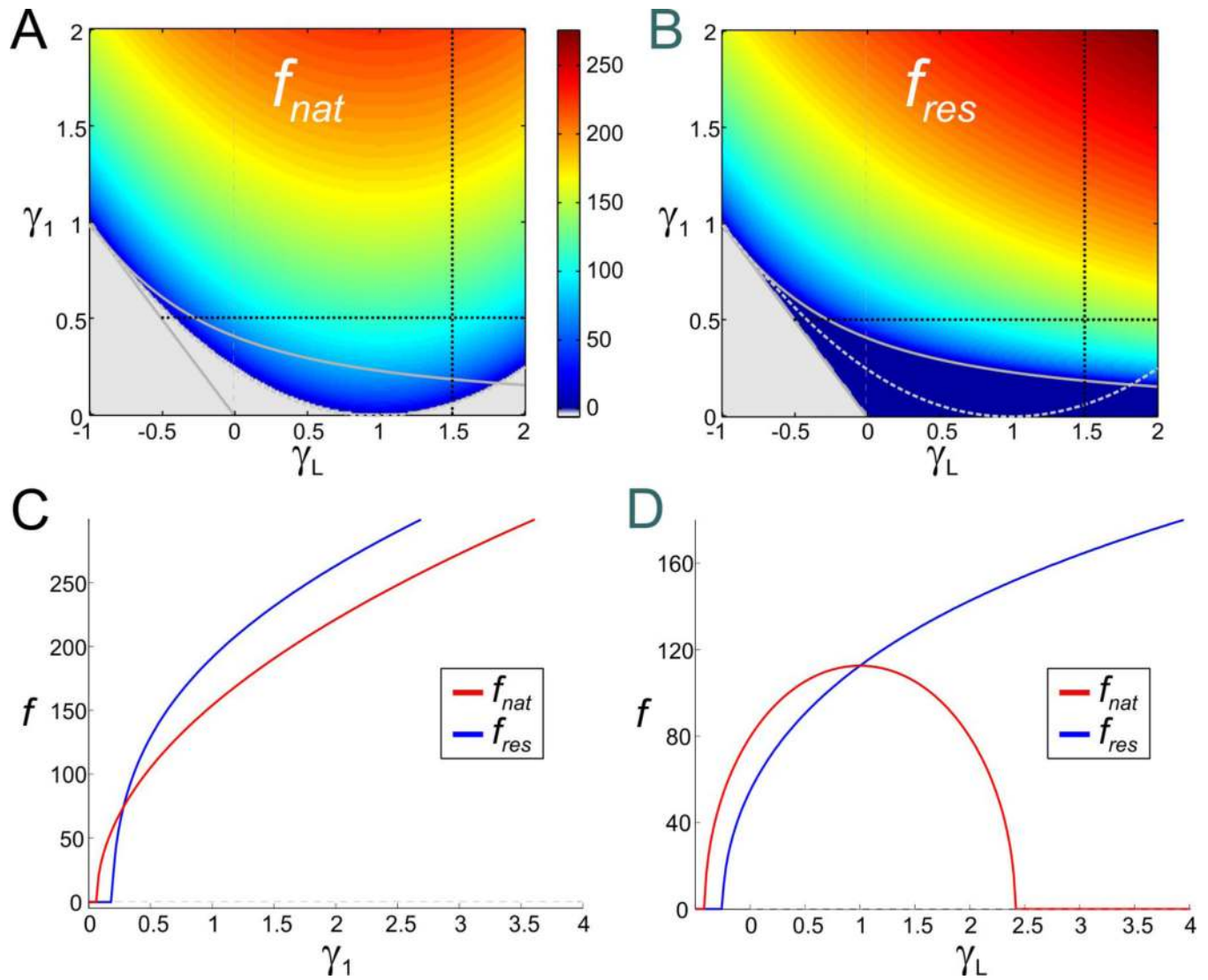
**Figure 2.**

Stability, oscillatory, and resonant properties for the 2D linear system (6) With  $C = 1$  and  $\tau_1 = 1$  in the  $g_L - g_1$  space. (For these parameters values,  $g_1 = \gamma_1$  and  $g_L = \gamma_L$  and the 2D linear (6) and the 2D rescaled system (10) are equivalent.) **A1.** Superimposed stability and resonance diagrams. The blue curves separate between regions in parameter space with different stability properties or fixed point types. Symbols indicate whether the fixed point is a focus, node or saddle (blue symbols stable; red symbols unstable). The green curve (resonance curve; obtained from Eq. (22); see Results) separates between regions in

parameter space where the system exhibits resonance (green) or does not (other). **A2.** A magnification of A1 (yellow dotted box). All regions above the grey saddle region are stable. **B. to D.** Representative examples of impedance profiles for the rescaled system (10) with  $\gamma_1$  and  $\gamma_L$  values denoted in the figure. Black dots and lines denote the resonant points.

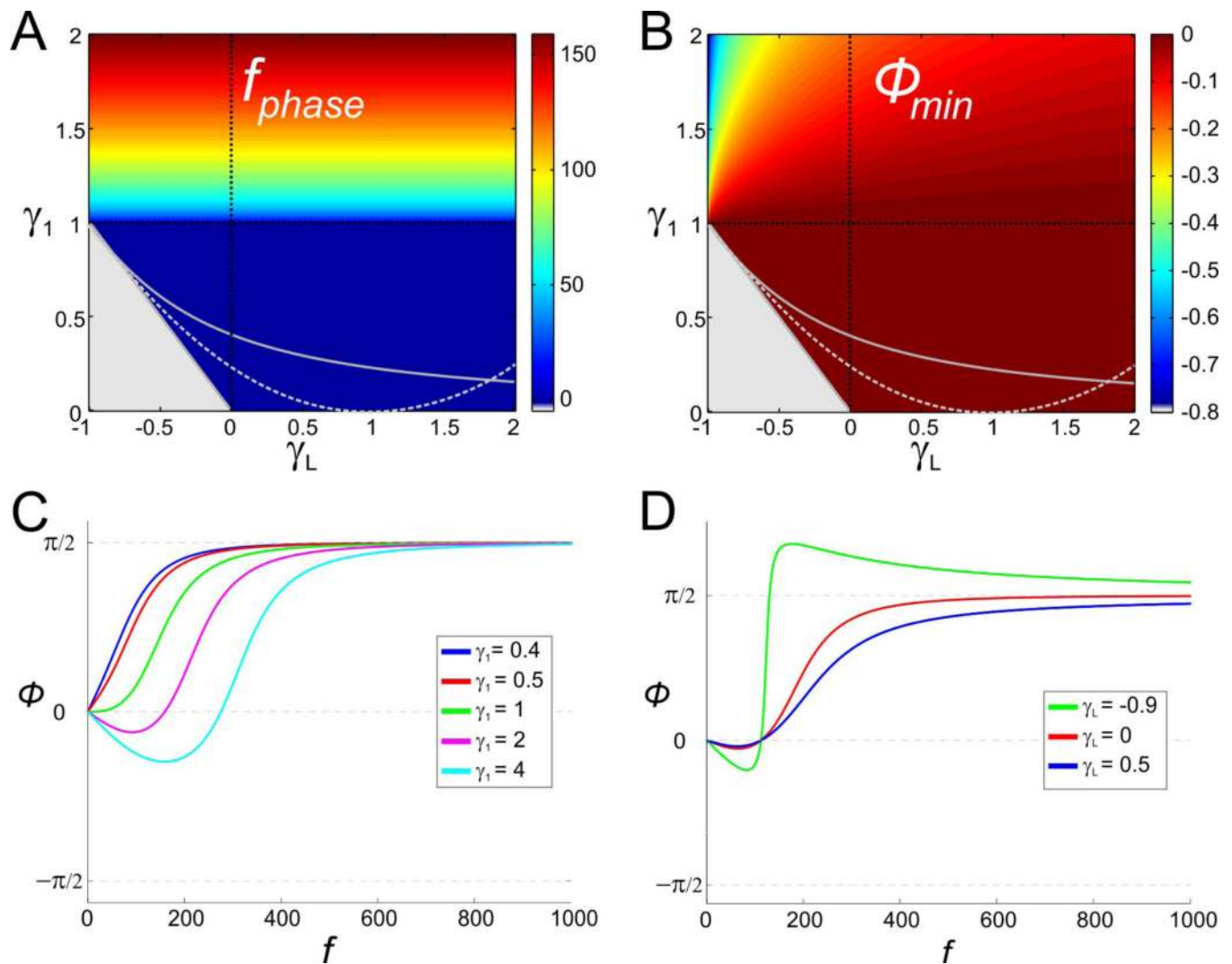
**Figure 3.**

The attributes of resonance for the 2D linear system (6) (as in Fig. 2). **A.** The maximum impedance  $Z_{max}$ . **B.** The zero-frequency input resistance  $Z(0)$  (same scale as A). Dark red regions in A and B are outside the scale of the graph. Gray region and curves as in Fig. 2A2. Inset shows  $Q_Z$  (the difference between  $Z_{max}$  and  $Z(0)$ ) in the same range of  $\gamma_1$  and  $\gamma_L$ . **C.** Representative example of  $Z_{max}$  and  $Z(0)$  as a function of  $\gamma_1$  for  $\gamma_L = 0$  (vertical dashed black line in A and B). **D.** Representative example of  $Z_{max}$  and  $Z(0)$  as a function of  $\gamma_L$  for  $\gamma_1 = 1$  (horizontal dashed black line in A and B). **E.** Half band-width  $\Lambda_{1/2}$ . **F.** Representative example of  $\Lambda_{1/2}$  as a function of  $\gamma_1$  for  $\gamma_L = 0$  (vertical dashed black line in E). **G.** Representative example of  $\Lambda_{1/2}$  as a function of  $\gamma_L$  for  $\gamma_1 = 1$  (horizontal dashed black line in E).



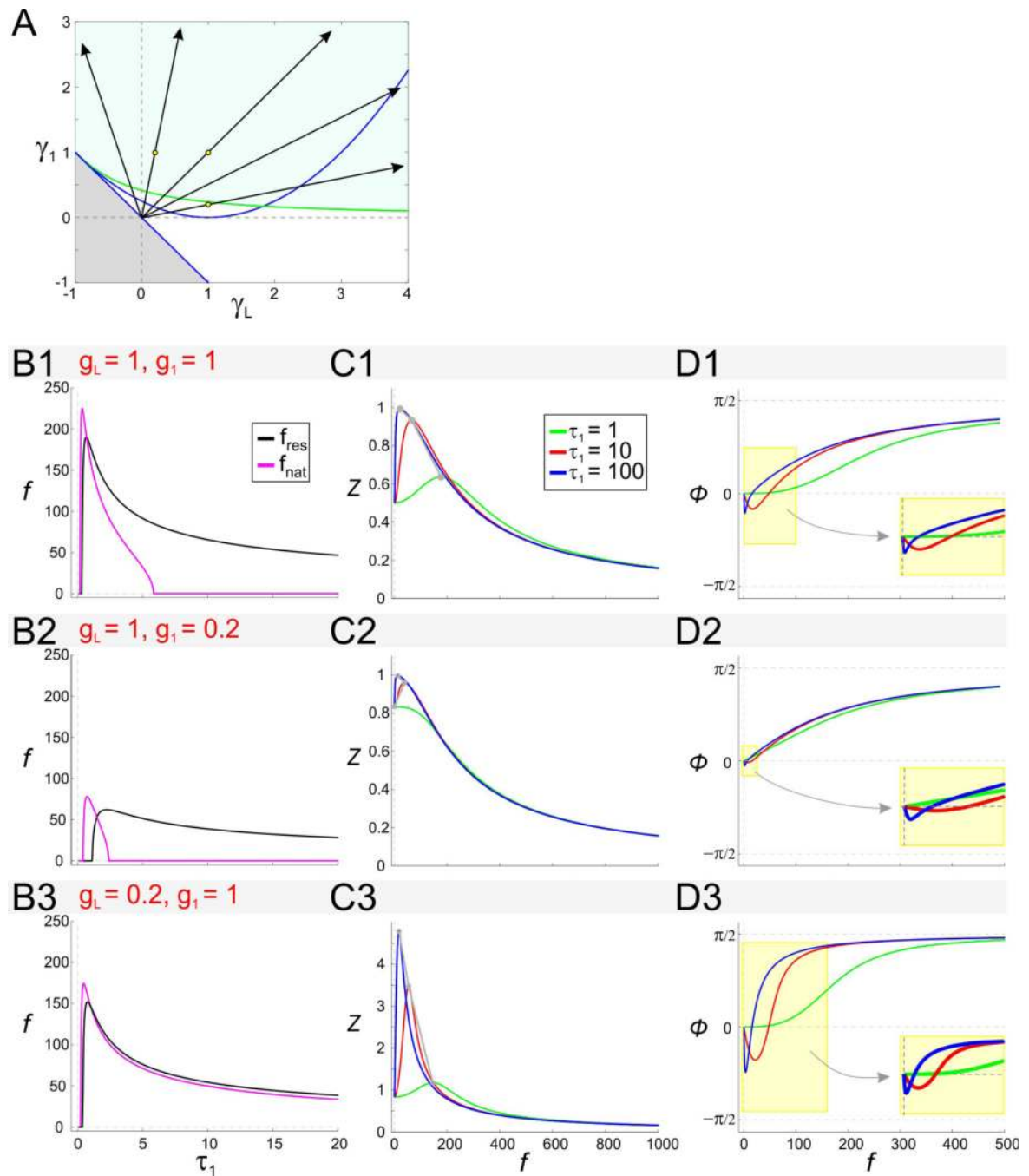
**Figure 4.** Natural and resonant frequency color bar diagrams for the 2D linear system (6) (as in Fig. 2). **A.** Natural frequency  $f_{nat}$ . **B.** Resonant frequency  $f_{res}$  (same scale as A). Gray region and curves as in Fig. 2A2. **C.** Representative example of  $f_{res}$  and  $f_{nat}$  as a function of  $\gamma_1$  for  $\gamma_L = 1.5$  (vertical dashed black lines in A and B). **D.** Representative example of  $f_{res}$  and  $f_{nat}$  as a function of  $\gamma_L$  for  $\gamma_1 = 0.5$  (horizontal dashed black lines in A and B).



**Figure 5.**

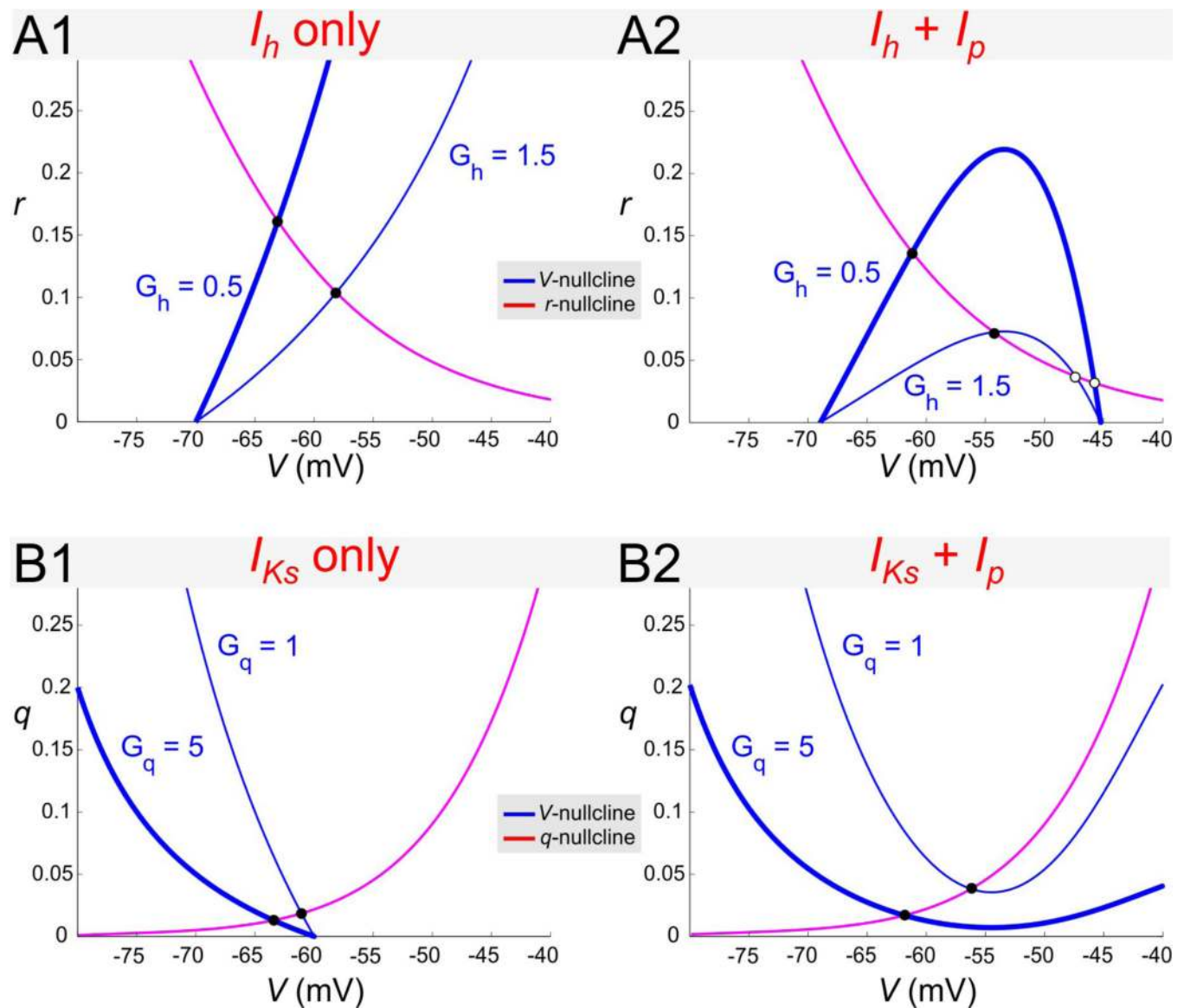
Negative-phase-frequency-band for the 2D linear system (6) (as in Fig. 2). **A.** The length of the negative-phase-frequency band (or, equivalently, the zero-phase-frequency  $f_{phase}$ ). **B.** Minimum phase ( $\phi_{min}$ ) of the voltage response. Gray region and curves as in Fig. 2A2. **C.** Representative example of the phase profile as a function of  $\gamma_1$  for  $\gamma_L = 0$  (vertical dashed black line in A and B). **D.** Representative example of the phase profile as a function of  $\gamma_L$  for  $\gamma_1 = 1$  (vertical dashed black line in A and B).



**Figure 6.**

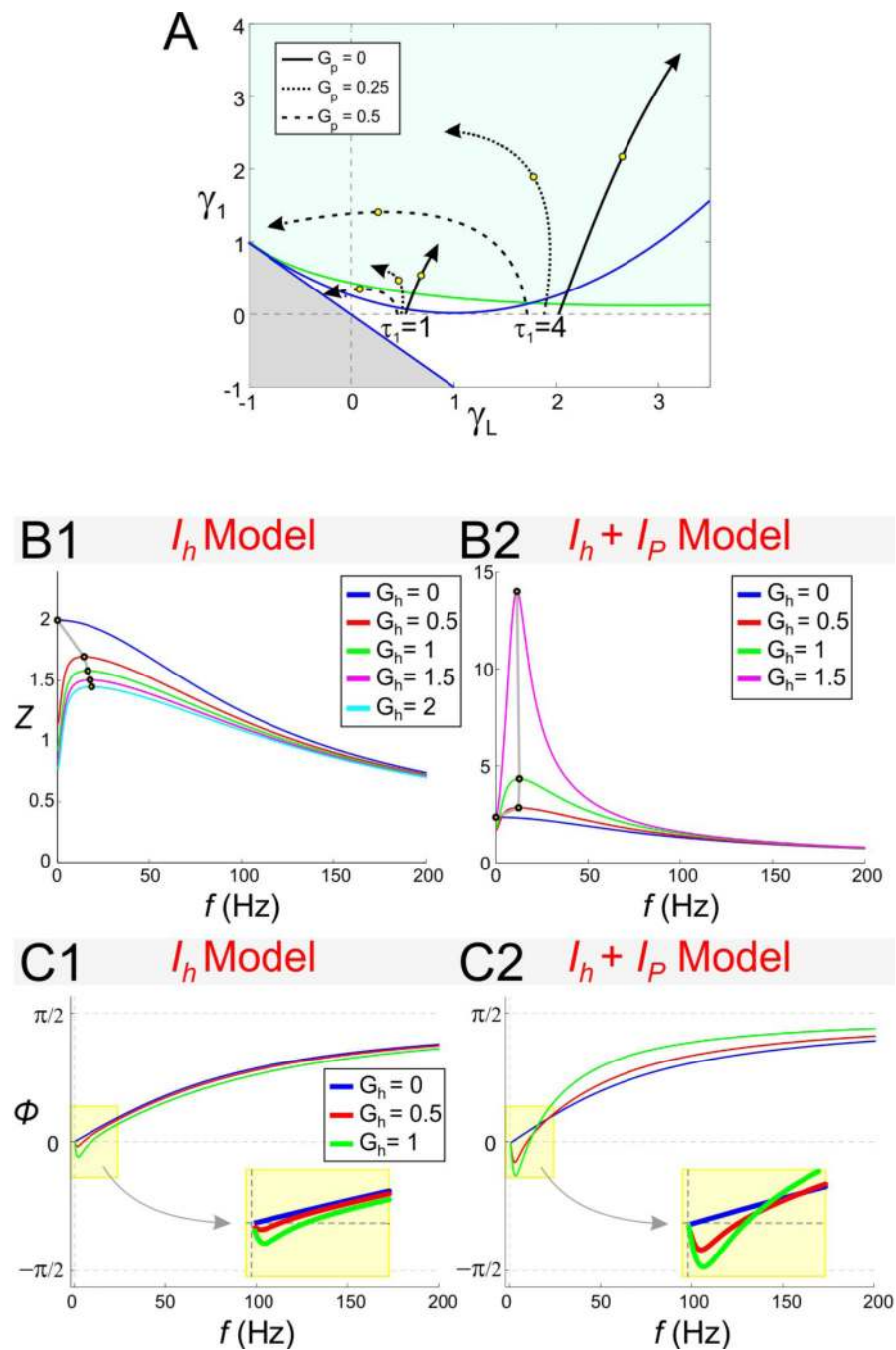
The effect of the time constant  $\tau_1$  on impedance and phase in the linear model. **A.** The effect of  $\tau_1$  on the rescaled conductances  $\gamma_L$  and  $\gamma_1$ . The region shown is as in Fig. 2A2. For fixed values of the conductances  $g_1$  and  $g_L$ , as  $\tau_1$  increases, the rescaled effective conductances  $\gamma_1$  and  $\gamma_L$  increase along lines emanating from the origin. **B.** Resonant and natural frequencies of the 2D linear system as a function of  $\tau_1$  for representative values of  $g_1$  and  $g_L$ . **C.** Impedance profiles for representative values of  $g_1$  and  $g_L$  with different values of  $\tau_1$  (as shown in C1). **D.** Phase profiles for representative values of  $g_1$  and  $g_L$  with different values

of  $\tau_1$  (as shown in C1). Insets show expansions of the shaded box and demonstrate that increasing  $\tau_1$  moves the zero-phase-frequency to smaller values.



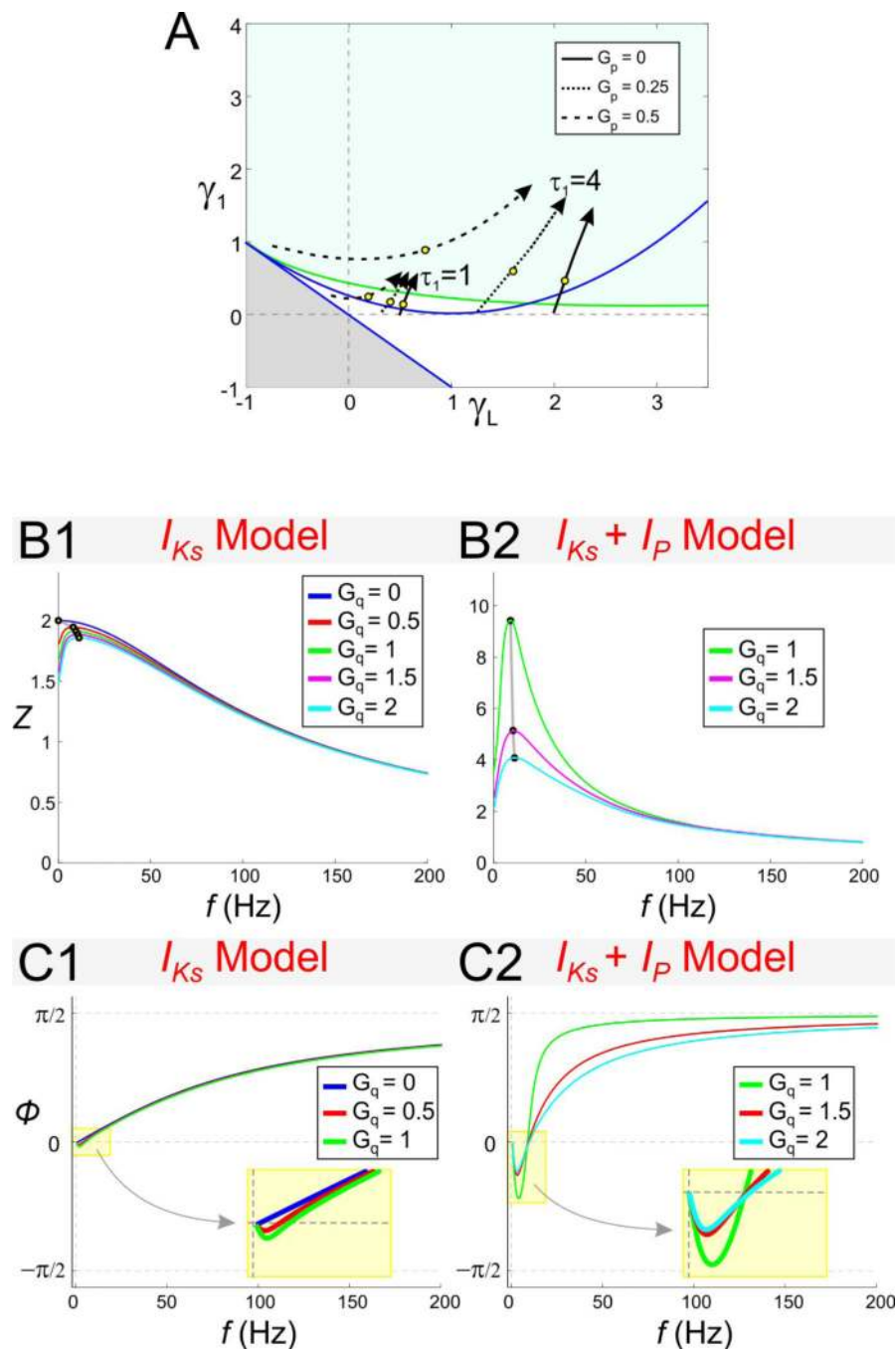
**Figure 7.**

Nullclines for different 2D biophysical models. **A.** In the  $I_h + I_p$  model with  $G_p = 0$  (**A1**) different values of  $G_h$  lead to nullclines that are close to linear near the fixed point. In contrast, when  $G_p > 0$  (**A2**;  $G_p = 0.5$ ) the V-nullcline can show quadratic nonlinearities near the fixed point. **B.** Similarly in the  $I_M + I_p$  model with  $G_p = 0$  (**B1**) the nullclines are close to linear whereas when  $G_p > 0$  (**B2**;  $G_p = 0.5$ ) the V-nullcline shows quadratic nonlinearities. Note that the individual nullclines are qualitatively mirror images of those of the  $I_h + I_p$  model. In all panels filled circles denote stable fixed points and open circles denote saddle points.

**Figure 8.**

The effect of  $G_h$  on resonance and zero-phase-frequency in the  $I_h + I_p$  model. **A.** Trajectories in  $\gamma_L - \gamma_1$  space parameterized by the resonant conductance  $G_h$  (arrows indicate increasing values of  $G_h$ ). All trajectories start at  $G_h = 0$  and the value  $G_h = 1.5$  is marked by an open circle. Different trajectories correspond to different representative values of  $G_p$  and  $\tau_1$  (as indicated). The trajectories are computed until the fixed-point  $V$  ceases to exist. Gray region and curves as in Fig. 2A2. **B.** Impedance profiles for the linearized  $I_h + I_p$  model with  $G_p = 0$

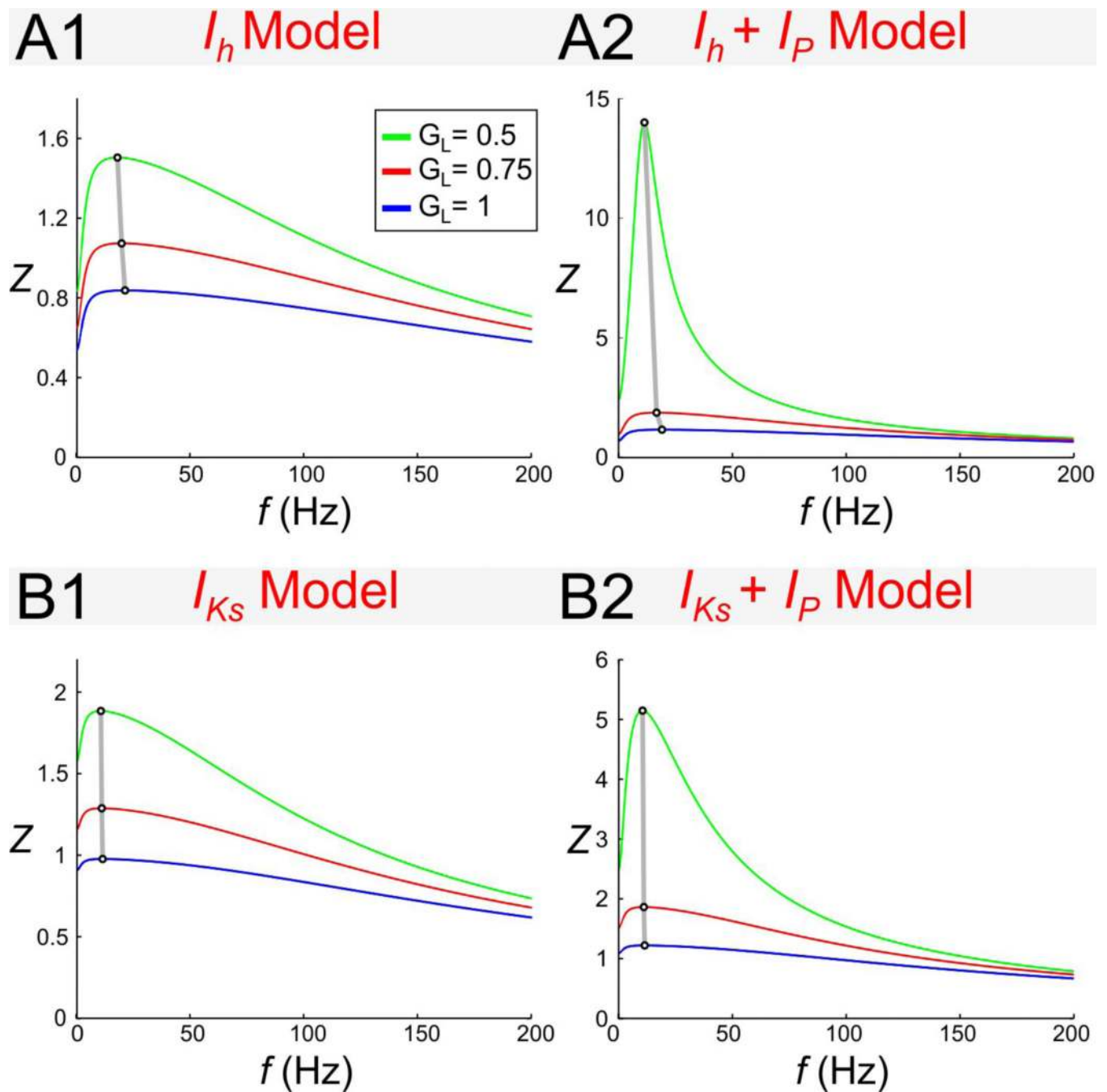
(**B1**) and  $G_p = 0.5$  (**B2**). **C.** Phase profiles for the linearized  $I_h + I_p$  model with  $G_p = 0$  (**C1**) and  $G_p = 0.5$  (**C2**). In **B** and **C**  $I_{app} = -2.5$ .

**Figure 9.**

The effect of  $G_q$  on resonance frequency in the  $I_{Ks} + I_p$  model. **A.** Trajectories in  $\gamma_L - \gamma_1$  space parameterized by the resonant conductance  $G_q$  (arrows indicate decreasing values of  $G_q$ ). Each trajectory starts at the value of  $G_q$  at which the two nullclines first intersect and  $V$  emerges. The end of each trajectory marks  $G_q = 3$  in all cases and open circles mark  $G_q = 1$ . Different trajectories correspond to different representative values of  $G_p$  and  $\tau_1$  (as indicated). Gray region and curves as in Fig. 2A2. **B.** Impedance profiles for the linearized

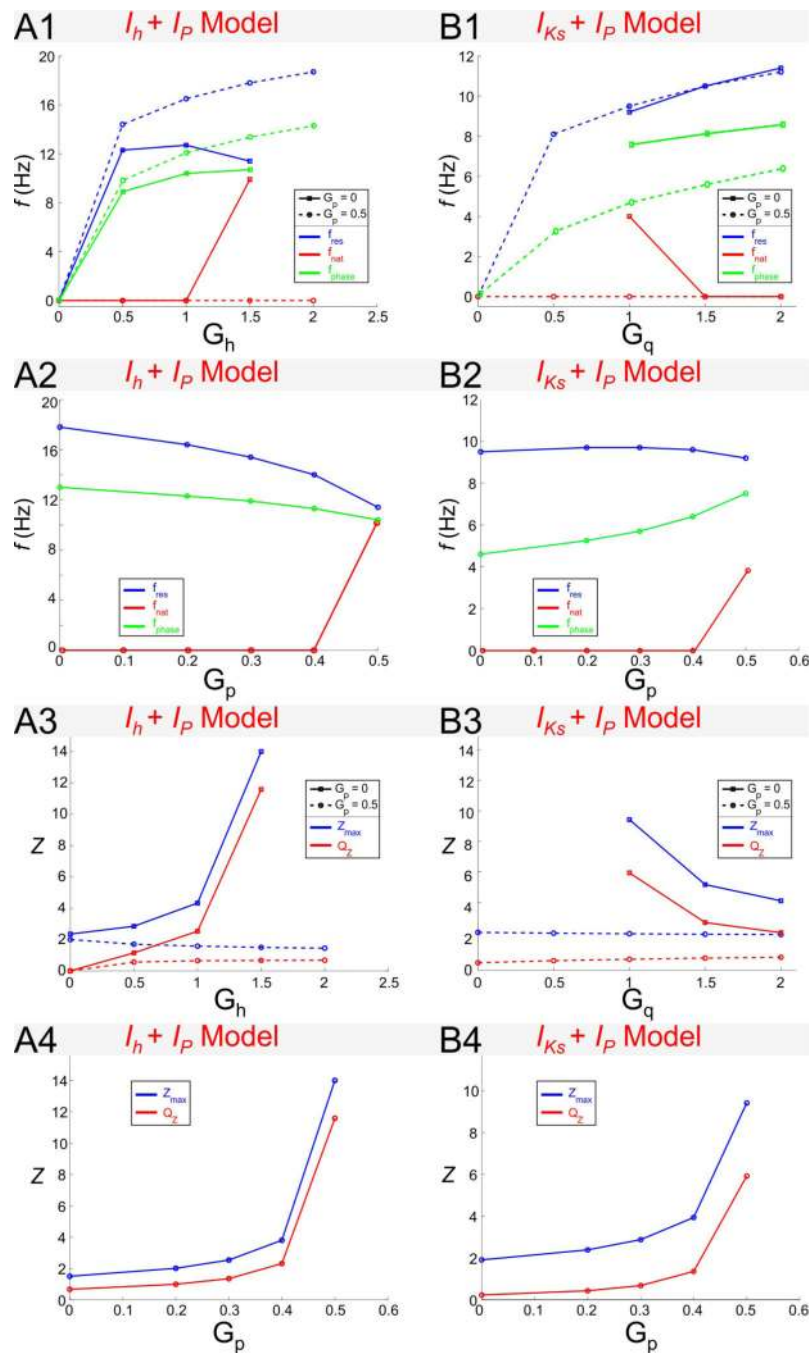
$I_{KS} + I_p$  model with  $G_p = 0$  (**B1**) and  $G_p = 0.5$  (**B2**). **C.** Phase profiles for the linearized  $I_{KS} + I_p$  model with  $G_p = 0$  (**C1**) and  $G_p = 0.5$  (**C2**). In **B** and **C**  $I_{app} = 2.5$ .



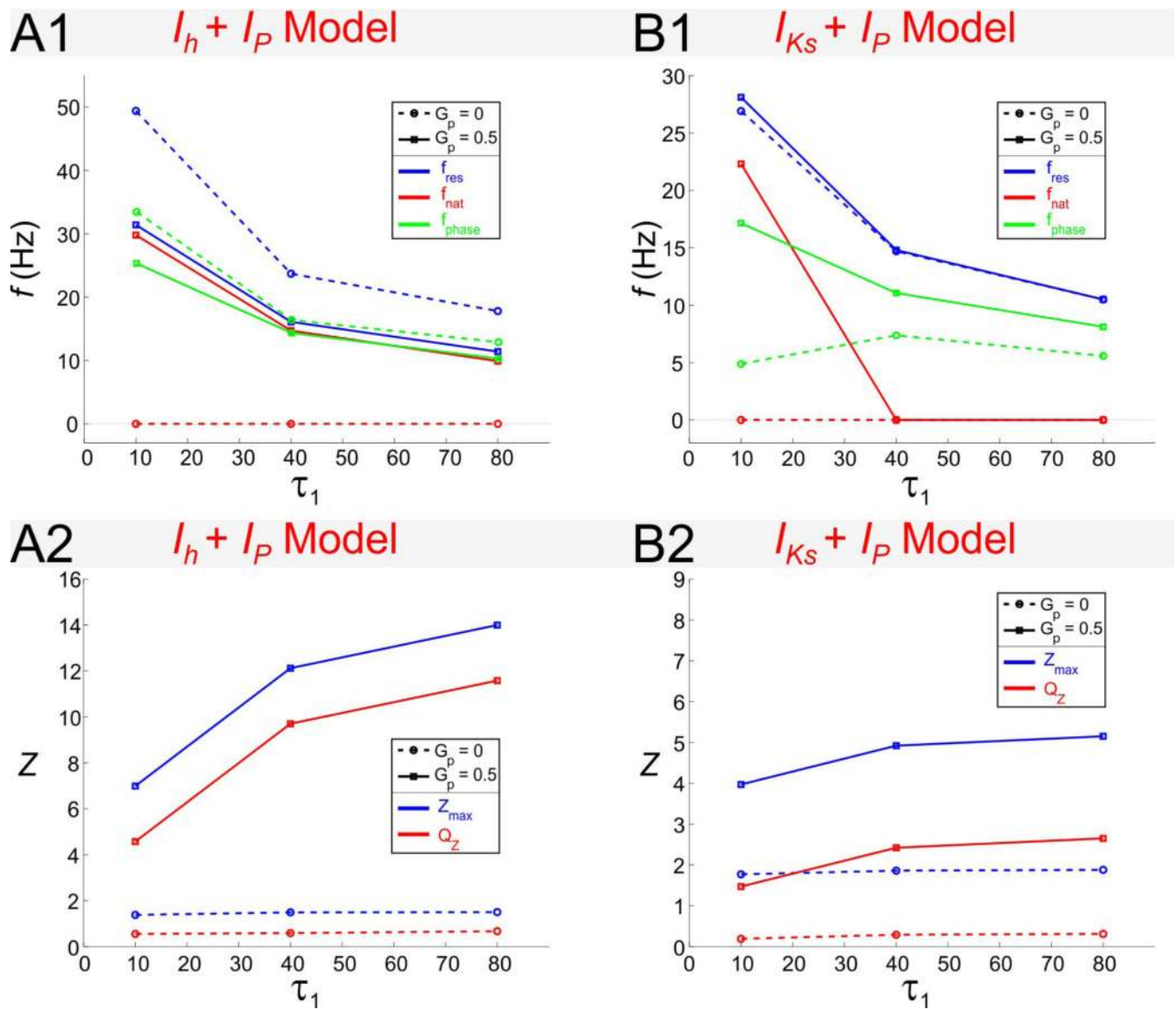


**Figure 10.**

The effect of  $G_L$  on resonance frequency in the  $I_h + I_p$  and  $I_{Ks} + I_p$  models. **B.** Impedance profiles for the linearized  $I_h + I_p$  model with  $G_p = 0$  (**B1**) and  $G_p = 0.5$  (**B2**) and  $G_h = 1.5$ . **C.** Impedance profiles for the linearized  $I_{Ks} + I_p$  model with  $G_p = 0$  (**C1**) and  $G_p = 0.5$  (**C2**) and  $G_q = 1.5$ . In all panels  $I_{app} = 2.5$ . Figure legend in A1 applies to all panels.

**Figure 11.**

Dependence of resonance and phase properties for the  $I_h + I_p$  (column A) and  $I_{Ks} + I_p$  (column B) models on the maximal conductances. Panels A1 and B1 show  $f_{res}$ ,  $f_{nat}$  and  $f_{phase}$  as a function of  $G_h$  (A1) or  $G_q$  (B1) with  $G_p = 0$  or  $G_p = 0.5$ . Panels A2 and B2 show  $f_{res}$ ,  $f_{nat}$  and  $f_{phase}$  as a function of  $G_p$ . Panels A3 and B3 show  $Z_{max}$  and  $Q_Z$  as a function of  $G_h$  (A3) or  $G_q$  (B3).  $f_{res}$  and  $f_{nat}$  as a function of  $G_q$ . Panels A4 and B4 show  $Z_{max}$  and  $Q_Z$  as a function of  $G_p$ .  $I_{app} = -2.5$  for the  $I_h + I_p$  model and  $I_{app} = 2.5$  for the  $I_{Ks} + I_p$  model. The time constant  $\tau_1 = 80$  for both models.

**Figure 12.**

Dependence of resonance and phase properties for the  $I_h + I_p$  (column **A**) and  $I_{Ks} + I_p$  (column **B**) models on the time constant  $\tau_1$ . Panels **A1** and **B1** show  $f_{res}$ ,  $f_{nat}$  and  $f_{phase}$  as a function of  $\tau_1$ . Panels **A2** and **B2** show  $Z_{max}$  and  $Q_Z$  as a function of  $\tau_1$ .  $I_{app} = -2.5$  for the  $I_h + I_p$  model and  $I_{app} = 2.5$  for the  $I_{Ks} + I_p$  model. The time constant  $\tau_1 = 80$  for both models.